1

Energetic bounds on gyrokinetic instabilities. Part 4. Bounce-averaged electrons

P.J. Costello [1],† and G.G. Plunk [1]

[1]Max-Planck-Institut für Plasmaphysik, Wendelsteinstraße 1, 17491 Greifswald, Germany

Upper bounds on the growth of instabilities in gyrokinetic systems have recently been derived by considering the optimal perturbations that maximise the growth of a chosen energy norm. This technique has previously been applied to two-species gyrokinetic systems with fully kinetic ions and electrons. However, in tokamaks and stellarators, the expectation from linear instability analyses is that the most important kinetic electron contribution to ion-scale modes often comes from the trapped electrons, which bounce faster than the time scale upon which instabilities evolve. As a result, a fully kinetic electron response is not required to describe unstable modes in many cases. Here, we apply the optimal mode analysis to a reduced two-species system consisting of fully gyrokinetic ions and bounce-averaged electrons, with the aim of finding a tighter bound on ion-scale instabilities in toroidal geometry. This analysis yields bounds that are greatly reduced in comparison with the earlier two-species result. Moreover, if the energy norm is properly chosen, wave–particle resonance effects can be captured, reproducing the stabilisation of density-gradient-driven instabilities in maximum-*J* devices. The optimal mode analysis also reveals that the maximum-*J* property has an additional stabilising effect on ion-temperature-gradient-driven instabilities, even in the absence of an electron free energy source. This effect is explained in terms of the concept of mode inertia, making it distinct from other mechanisms.

---

1. Introduction

In a recent series of papers (Helander & Plunk 2021, 2022; Plunk & Helander 2022, 2023) a new theory has been developed that bounds the growth of linear and nonlinear instabilities in gyrokinetic systems by considering the energy balance that must be obeyed by these systems (from now on we will refer to these publications as Parts 1, 2 and 3, respectively). These upper bounds are attained by the optimal modes of the system – states of the gyrokinetic system that maximise the growth of a chosen 'energy norm' within the limits allowed by energy balance. The optimal modes form a complete orthogonal basis for the space of distribution functions. Unlike the 'normal' modes of the linear gyrokinetic operator (solutions to the gyrokinetic system which evolve as $\exp(-i\omega t)$), the velocity

---

† Email address for correspondence: paul.costello@ipp.mpg.de

space dependence of the optimal modes is significantly simpler. Moreover, the optimal modes possess a closed-form solution in terms of a finite set of gyrofluid-like moments, without any closure approximation, resulting in a low-dimensionality eigenvalue problem for the optimal growth rate, which can be solved at low computational cost. This makes the optimal modes an attractive lens with which to explore gyrokinetic systems.

There is a wide range of energy norms that can be used in these optimal mode analyses. In Parts 1 and 2 the bounds were developed using the Helmholtz free energy as an energy norm, culminating in upper bounds on fully electromagnetic, multispecies instabilities. Part 3 extended the optimal mode analysis by considering the generalised free energy, a linear combination of the Helmholtz free energy and the electrostatic energy, for a single kinetic species (kinetic ions with adiabatic electrons). The optimal growth of this generalised free energy yields the lowest possible upper bound that can be formed from the balance of these two energies, as will become clearer below. Importantly, the generalised free energy adds an explicit dependence on magnetic geometry into the optimal mode analysis by retaining the wave–particle interaction effects, including magnetic drifts, which contribute in a physically transparent way to the evolution of the field energy of the system.

While the bounds derived for the system with kinetic ions and adiabatic electrons have been found to be quite close to the results of linear gyrokinetic simulations in tokamaks and stellarators, the upper bounds for two kinetic species in the electrostatic limit derived in Part 2 tends to be several times larger than the simulated linear instability growth in these geometries (Podavini *et al.* 2025). This is most evident at small values of the perpendicular wavenumber $k_\perp$, where the simulated growth rates in the toroidal geometries tend to zero, and the upper bound tends to a non-zero value of considerable size. This discrepancy in qualitative behaviour is because the upper bound of Part 2 is geometry independent and must also bound the growth of instabilities in closed-field-line geometries, like the *z*-pinch (Ricci *et al.* 2006), which exhibit finite growth as $k_\perp \to 0$. As we will see, the difference in these geometries lies in the transit average of the passing-electron response, which may be non-adiabatic in closed-field-line geometry but is largely adiabatic on the typical instability time scale in toroidal geometry, where the trapped electrons dominate the non-adiabatic electron response.

In this work, we aim to increase the applicability of the optimal mode theory with a kinetic electron response to stellarator and tokamak geometry. This is done by considering a reduced two-species system, in the electrostatic limit, in which the electron transit time along the magnetic field is assumed to be much faster than the evolution of the instabilities. In toroidal geometry, this eliminates the passing-electron contribution to instabilities, at lowest order, leaving only a bounce-averaged trapped electron response. The resulting gyrokinetic system is often used to describe electrostatic instabilities such as trapped-electron modes (TEMs) (Helander, Proll & Plunk 2013) and ion-driven TEMs (ITEMs) (Plunk, Connor & Helander 2017), but is also applicable to ion-temperature gradient modes (ITGs) (Proll *et al.* 2022). We note that we exclude modes such as the electron-temperature-gradient mode (ETG) (Dorland *et al.* 2000; Plunk *et al.* 2019) and the universal mode (Helander & Plunk 2015; Landreman, Plunk & Dorland 2015) which evolve on time scales comparable to, or shorter than, the electron transit time.

To include wave–particle resonance effects, particularly involving the magnetic drifts, we construct the generalised free energy (of which the Helmholtz free energy is a special case) of the system with gyrokinetic ions and bounce-averaged electrons. We first study the Helmholtz free energy limit, which is directly comparable with the two-species result of Part 2. We then consider the full generalised free energy and explore the impact of magnetic curvature on the optimal modes and the resulting upper bounds. We confirm

that the previously known linear stability benefits of maximum-*J* magnetic geometries associated with the presence of an electron free energy source (Proll *et al.* 2012; Helander *et al.* 2013) are exhibited by the optimal modes. The optimal mode analysis also reveals an additional stabilising effect that the maximum-*J* property has on ITGs – even in the absence of an electron free energy source. We explain this effect through the concept of mode inertia, which is sensitive to the degree of depletion of the Boltzmann response by the trapped electrons. This is distinct from other mechanisms described in previous works that enhance microstability in maximum-*J* stellarators, which involve a lack of resonance between bounce-averaged curvature and diamagnetic drifts.

2. Gyrokinetic system

To begin, we consider a local, electrostatic gyrokinetic system, where the domain is a narrow flux tube centred around a magnetic field line in the plasma. In this local approximation, a Fourier decomposition may be applied in the directions perpendicular to the magnetic field assuming periodicity in these coordinates. The electrostatic gyrokinetic equation for a species a, and the Fourier component $\boldsymbol{k}$ is

$$\frac{\partial g_{a,k}}{\partial t} + v_\parallel \frac{\partial g_{a,k}}{\partial l} + \mathrm{i}\omega_{\mathrm{da}} g_{a,k} + \frac{1}{B^2} \sum_{k'} \boldsymbol{B} \cdot (\boldsymbol{k} \times \boldsymbol{k}') \delta\phi_{k'} \mathrm{J}_{0a}\, g_{a,k-k'}$$
$$= \frac{e_a F_{a0}}{T_a} \left(\frac{\partial}{\partial t} + \mathrm{i}\omega_{*a}^T \right) \delta\phi_k \mathrm{J}_{0a}, \tag{2.1}$$

where $g_{a,k}$ is the non-adiabatic part of the perturbed distribution function $g_a(\boldsymbol{R}, E_a, \mu_a, t)$ $= \delta f(\boldsymbol{r}, \boldsymbol{v}, t) + e_a \delta\phi(\boldsymbol{r}, t) F_{a0}/T_a$, F_{a0} is the background Maxwellian distribution and $\delta\phi$ is the electrostatic potential. The phase-space coordinates for the gyrocentre distribution function g_a are the magnetic moment, $\mu_a = m_a v_\perp^2/(2B)$ and the kinetic energy, $E_a = m_a v^2/2$. We also use Clebsch magnetic coordinates, in which the magnetic field is of the form $\boldsymbol{B} = \nabla\psi \times \nabla\alpha$, where ψ is the toroidal magnetic flux (acting as a radial coordinate in toroidal geometry), and α is the binormal coordinate, which labels different field lines on surfaces of constant ψ. In these coordinates, the field-line following coordinate is l, the unit vector along the magnetic field is $\boldsymbol{b} = \boldsymbol{B}/B$ and the perpendicular wavenumber is $\boldsymbol{k} = \boldsymbol{k}_\perp = k_\alpha \nabla\alpha + k_\psi \nabla\psi$. The argument of the Bessel function is $\mathrm{J}_0 = \mathrm{J}_0(k_\perp v_\perp/\Omega_a)$ with the gyrofrequency defined as $\Omega_a = e_a B/m_a$. The magnetic drift frequency is $\omega_{da} = \boldsymbol{k}_\perp \cdot \boldsymbol{v}_d$, where $\boldsymbol{v}_d = \boldsymbol{b} \times (v_\perp^2/2\nabla\ln B + v_\parallel^2 \boldsymbol{\kappa})/\Omega_a$. In the low-plasma pressure limit (assuming $\nabla\ln B \approx \boldsymbol{\kappa}$), the drift frequency can be approximated by

$$\omega_{\mathrm{da}} \approx \hat{\omega}_{\mathrm{da}}(l) \left(\frac{v_\perp^2}{2v_{\mathrm{Ta}}^2} + \frac{v_\parallel^2}{v_{\mathrm{Ta}}^2} \right), \tag{2.2}$$

where $v_{\mathrm{Ta}} = \sqrt{2T_a/m_a}$ is the thermal speed and $\hat{\omega}_{\mathrm{da}}(l)$ is a geometry dependent factor. The energy-dependent diamagnetic drift frequency is

$$\omega_a^T = \omega_{*a} \left[1 + \eta_a \left(\frac{v^2}{v_{\mathrm{Ta}}^2} - \frac{3}{2} \right) \right], \tag{2.3}$$

where the plasma gradients enter via $\omega_{*a} = (k_\alpha T_a/e_a)\, \mathrm{d}\ln n_a/\mathrm{d}\psi$ and the gradient ratio $\eta_a = \mathrm{d}\ln T_a/\mathrm{d}\ln n_a$. In the electrostatic limit, the system is closed by the quasineutrality

condition

$$\sum_a \frac{e_a^2 n_a}{T_a} \delta\phi_k = \sum_a e_a \int g_{a,k} J_{0a} \, \mathrm{d}^3 v. \tag{2.4}$$

In Clebsch coordinates, we may write the nonlinear term of (2.1) in the more convenient form

$$\frac{1}{B^2} \sum_{k'} \boldsymbol{B} \cdot (\boldsymbol{k} \times \boldsymbol{k'}) \delta\phi_{k'} J_{0a} \, g_{a,k-k'} = \sum_{k'} \left(k_\psi k'_\alpha - k_\alpha k'_\psi \right) \delta\phi_{k'} J_{0a} \, g_{a,k-k'}. \tag{2.5}$$

3. Bounce-averaged electrons

To simplify the electron gyrokinetic equation, we employ a standard ordering. We assume that the time scale of the dynamics of interest in the gyrokinetic system τ_D (i.e. the growth time of an instability) is much longer than the time scale on which thermal electrons transit the typical parallel length scale of the system, such that $\tau_D \gg L/v_{\mathrm{Te}}$. Expanding the electron distribution in orders of $L/(v_{\mathrm{Te}}\tau_D)$ as $g_{e,k} = g_{e,k}^0 + g_{e,k}^1 \dots$ we find that, to leading order,

$$v_\parallel \frac{\partial g_{e,k}^0}{\partial l} = 0, \tag{3.1}$$

such that the lowest-order electron distribution function is constant along the magnetic field line. This, it turns out, is a highly consequential result of this ordering, and how it is interpreted is the key to tailoring the forthcoming optimal mode analysis to capture the behaviour of the electron response for ion-scale instabilities that satisfy our ordering in toroidal geometry.

The constancy of $g_e^0 = g_e^0(E_e, \mu_e, \psi, \alpha)$ in l implies that its value is entirely determined by the parallel boundary conditions. For the passing particles in toroidal geometry, and for $k_\alpha \neq 0$, the relevant boundary conditions are the so-called 'incoming' boundary conditions of ballooning space where

$$g_{e,k}(v_\parallel > 0, l = -\infty) = 0, \tag{3.2}$$

$$g_{e,k}(v_\parallel < 0, l = \infty) = 0. \tag{3.3}$$

As explained in an appendix by Plunk *et al.* (2014), these boundary conditions are required to preserve causality (Connor, Hastie & Taylor 1980), such that information from the boundary, which is infinitely far away, cannot be communicated in a finite time. Therefore, it must be the case that $g_e^0(k_\alpha \neq 0) = 0$ in the passing region of velocity space to satisfy the boundary conditions. For the $k_\alpha = 0$ component, ballooning space boundary conditions are not appropriate because there is no mechanism that should cause the mode to decay along the flux tube. Thus, for $k_\alpha = 0$ the electron distribution function has a zeroth-order contribution from the passing electrons.

The trapped particles on the other hand (in the absence of collisions), are confined to a limited region of ballooning space. As such, the appropriate boundary conditions for these particles are the 'turning-point' boundary conditions (Connor *et al.* 1980),

$$g_{e,k}(v_\parallel > 0, l = l_1) = g_{e,k}(v_\parallel < 0, l = l_1), \tag{3.4}$$

$$g_{e,k}(v_\parallel > 0, l = l_2) = g_{e,k}(v_\parallel < 0, l = l_2) \tag{3.5}$$

where $l_{1,2}$ are the bounce points for a particle defined by $\lambda B(l_{1,2}) = 1$, where λ is the particle pitch angle, $\lambda = v_\perp^2/(v^2 B)$. These boundary conditions can be satisfied with

$g_{e,k}^0 \neq 0$, and so, for $k_\alpha \neq 0$, only the trapped electrons contribute to the non-adiabatic electron response in this limit. Note that this is not the case in closed-field-line geometries where the parallel boundary conditions can be periodic, allowing $g_{e,k}^0$ to be non-zero in the passing region of velocity space to zeroth order.

At next order in $L/(v_{\text{Te}}\tau_D)$, we find

$$\frac{\partial g_{e,k}^0}{\partial t} + v_\parallel \frac{\partial g_{e,k}^1}{\partial l} + \mathrm{i}\omega_{\text{de}} g_{e,k}^0 + \sum_{k'} \left(k_\psi k_\alpha' - k_\alpha k_\psi'\right) \delta\phi_{k'} \mathrm{J}_{0e} g_{e,k-k'}^0$$

$$= -\frac{eF_{e0}}{T_e}\left(\frac{\partial}{\partial t} + \mathrm{i}\omega_{*e}^T\right)\delta\phi_k \mathrm{J}_{0e}. \tag{3.6}$$

We now define the bounce average as

$$\overline{(\ldots)} = \frac{\displaystyle\int_{l_1}^{l_2}(\ldots)\,\mathrm{d}l/v_\parallel}{\displaystyle\int_{l_1}^{l_2}\mathrm{d}l/v_\parallel} = \frac{1}{\tau_B}\int_{l_1}^{l_2}\frac{(\ldots)\,\mathrm{d}l}{\sqrt{1-\lambda B}}, \tag{3.7}$$

where we have introduced the bounce time $\tau_B = \int_{l_1}^{l_2}(\mathrm{d}l/\sqrt{1-\lambda B})$.[1] In pitch-angle coordinates, the velocity space element is defined as

$$\mathrm{d}^3v = \sum_\sigma \frac{\pi v^2 B\,\mathrm{d}v\,\mathrm{d}\lambda}{\sqrt{1-\lambda B}}, \tag{3.8}$$

where $\sigma = v_\parallel/|v_\parallel|$. Applying the bounce average to (3.6) annihilates the $g_{e,k}^1$ contribution, leaving an equation for $g_{e,k}^0$. Additionally ordering $k_\perp \rho_e \ll 1$, where $\rho_a = v_{\text{Ta}}/|\Omega_a|$, for simplicity and omitting the superscript '0' for brevity gives

$$\frac{\partial g_{e,k}}{\partial t} + \mathrm{i}\overline{\omega}_{\text{de}} g_{e,k} + \sum_{k'}\left(k_\psi k_\alpha' - k_\alpha k_\psi'\right)\overline{\delta\phi}_{k'}\,g_{e,k-k'} = -\frac{eF_{e0}}{T_e}\left(\frac{\partial}{\partial t} + \mathrm{i}\omega_{*e}^T\right)\overline{\delta\phi}_k. \tag{3.9}$$

We now consider (3.9) as the governing equation for the bounce-averaged electrons in our gyrokinetic system, which is accurate to lowest order in $L/(v_{\text{Te}}\tau_D)$. Here, we restrict our view to toroidal geometry such that, for $k_\alpha \neq 0$, g_e is only non-zero in the trapped region of velocity space.

4. Energy balance

In the limit of $\tau_D \gg L/v_{\text{Te}}$, we have a gyrokinetic system comprised of ions described by (2.1), with finite ion-Larmor-radius effects, and bounce-averaged electrons described by (3.9). As described in Parts 1, 2 and 3, we can construct energy norms for this two-species system that are conserved by the nonlinear terms of the gyrokinetic equations. These nonlinear invariants are the Helmholtz free energy, detailed in Parts 1 and 2, and the electrostatic energy, described in Part 3. We now derive these invariants in our system with bounce-averaged electrons.

---

[1]Here τ_B has units of length, due to the cancellation of v when changing to pitch-angle coordinates, but is typically referred to as the bounce time for trapped particles.

4.1. *Helmholtz free energy*

For simplicity, we will consider a two-species hydrogen plasma with $n_i = n_e = n$, but the following can be easily generalised to multiple ion species. Constructing the Helmholtz free energy of this system proceeds in the same manner as in the general multispecies case, shown in Part 2, except for our assumption that $k_\perp \rho_e \ll 1$. This is done by multiplying the gyrokinetic equation for each species by the factor $T_a g_{a,k}^* / F_{a0}$, integrating over velocity space, applying the flux-tube average defined by

$$\langle \ldots \rangle = \lim_{L \to \infty} \int_{-L}^{L} (\ldots) \frac{\mathrm{d}l}{B} \Big/ \int_{-L}^{L} \frac{\mathrm{d}l}{B} = \lim_{L \to \infty} \frac{1}{V} \int_{-L}^{L} (\ldots) \frac{\mathrm{d}l}{B}, \tag{4.1}$$

summing the equations for both species, and taking the real part. Applying the flux-tube average has no impact on the bounce-averaged electron equation, but we leverage the identity

$$\left\langle \int \overline{f(\boldsymbol{v}, l)} \, \mathrm{d}^3 v \right\rangle = \left\langle \int \overline{f(\boldsymbol{v}, l) \, \mathrm{d}^3 v} \right\rangle \tag{4.2}$$

to allow us to combine the electron and ion contributions to the Helmholtz free energy. After using quasineutrality, we arrive at the Helmholtz free energy, which looks similar to that of Parts 1 and 2,

$$H(\boldsymbol{k}, t) = \sum_a \left\langle T_a \int \frac{|g_{a,k}|^2}{F_{a0}} \mathrm{d}^3 v - \frac{e_a^2 n}{T_a} |\delta\phi_k|^2 \right\rangle. \tag{4.3}$$

The Helmholtz free energy balance reads, as before,

$$\sum_k \frac{\mathrm{d}}{\mathrm{d}t} H(\boldsymbol{k}, t) = 2 \operatorname{Re} \sum_{a,k} \left\langle e_a \int \mathrm{i}\omega_{*a}^T \delta\phi_k \mathrm{J}_{0a} g_{a,k}^* \, \mathrm{d}^3 v \right\rangle$$

$$= 2 \sum_k \left(D_i(\boldsymbol{k}, t) + D_e^{\mathrm{tr}}(\boldsymbol{k}, t) \right); \tag{4.4}$$

the only difference here is that we have considered the limit $\mathrm{J}_{0e} \approx 1$ and $g_e = g_e(E_e, \mu_e, \psi, \alpha)$ with $g_e = 0$ for $\lambda < 1/B_{\max}$. We have denoted the electron contribution with a 'tr' superscript to signify that only the trapped region of velocity space contributes. The total free energy drive for a given $\boldsymbol{k}$ is then given by $D(\boldsymbol{k}, t) = D_i(\boldsymbol{k}, t) + D_e^{\mathrm{tr}}(\boldsymbol{k}, t)$, which determines the rate at which the system can grow given the presence of gradients in the plasma.

4.2. *Electrostatic energy*

To construct the generalised free energy, as demonstrated for a single kinetic species in Part 3, we first need to derive the electrostatic energy balance of the system with bounce-averaged electrons. As shown in Appendix A of Part 3, the electrostatic energy balance equation of a multispecies system may be constructed by applying the operator

$$\operatorname{Re} \sum_k \left\langle \int e_a \delta\phi_k^* \mathrm{J}_{0a} (\ldots) \, \mathrm{d}^3 v \right\rangle \tag{4.5}$$

to the gyrokinetic equations for each species and summing over species. When this operator is applied to the electron equation, the nonlinear term is annihilated. This can

be shown by noticing that its contribution,

$$\text{Re} \sum_{k,k'} \left\langle \int \left(k_\psi k'_\alpha - k_\alpha k'_\psi\right) \delta\phi_k^* \overline{\delta\phi}_{k'} \, g_{e,k-k'} \, \mathrm{d}^3 v \right\rangle, \tag{4.6}$$

when expressed in pitch-angle coordinates (3.8) and using the identity (Helander *et al.* 2013)

$$\int_{-\infty}^{+\infty} \mathrm{d}l \int_{1/B_{\max}}^{1/B(l)} \mathrm{d}\lambda \rightarrow \int_{1/B_{\max}}^{1/B_{\min}} \mathrm{d}\lambda \sum_j \int_{l_{1,j}}^{l_{2,j}} \mathrm{d}l, \tag{4.7}$$

where the subscript j denotes the different magnetic trapping wells along the flux tube, becomes

$$\text{Re} \sum_{k,k',\sigma,j} \frac{\pi}{V} \int_{1/B_{\max}}^{1/B_{\min}} \mathrm{d}\lambda \, \tau_{B,j} \int_0^\infty \mathrm{d}v \, v^2 \left(k_\psi k'_\alpha - k_\alpha k'_\psi\right) \overline{\delta\phi}_k^* \overline{\delta\phi}_{k'} \, g_{e,k-k'}. \tag{4.8}$$

Since $\delta\phi_k^* = \delta\phi_{-k}$ and $g_{e,k}^* = g_{e,-k}$, upon taking the real part, this contribution is proportional to

$$\left(k_\psi k'_\alpha - k_\alpha k'_\psi\right) \left(\overline{\delta\phi}_{-k} \overline{\delta\phi}_{k'} \, g_{e,k-k'} + \overline{\delta\phi}_k \overline{\delta\phi}_{-k'} \, g_{e,-k+k'}\right) \tag{4.9}$$

which changes sign if k and k' are swapped, such that this term vanishes upon summation over k and k'.

What remains of the electron equation when this operator is applied is

$$\text{Re} \sum_k \left\langle \int -e\delta\phi_k^* \left(\frac{\partial g_{e,k}}{\partial t} + i\overline{\omega}_{\mathrm{de}} g_{e,k}\right) \mathrm{d}^3 v \right\rangle$$
$$= \text{Re} \sum_k \left\langle \frac{e^2}{T_e} \int F_{e0} \delta\phi_k^* \left(\frac{\partial}{\partial t} + i\omega_{*e}^T\right) \overline{\delta\phi}_k \, \mathrm{d}^3 v \right\rangle. \tag{4.10}$$

We may also use the identity (4.7) to rewrite the right-hand side of this expression. Upon taking the real part of the right-hand side, the term proportional to ω_{*e}^T vanishes leaving

$$\text{Re} \sum_k \left\langle \int -e\delta\phi_k^* \left(\frac{\partial g_{e,k}}{\partial t} + i\overline{\omega}_{\mathrm{de}} g_{e,k}\right) \mathrm{d}^3 v \right\rangle = \frac{1}{4V} \frac{\mathrm{d}}{\mathrm{d}t} \sum_k \frac{e^2 n}{T_e} \sum_j \int_{1/B_{\min}}^{1/B_{\max}} \tau_{B,j} |\overline{\delta\phi}_{k,j}|^2 \, \mathrm{d}\lambda. \tag{4.11}$$

Applying the operator (4.5) to the ion gyrokinetic equation proceeds similarly, albeit without bounce averages, yielding

$$\text{Re} \sum_k \left\langle \int e\delta\phi_k^* \mathrm{J}_{0i} \left(\frac{\partial g_{i,k}}{\partial t} + v_\parallel \frac{\partial g_{i,k}}{\partial l} + i\omega_{\mathrm{di}} g_{i,k}\right) \mathrm{d}^3 v \right\rangle = \frac{\mathrm{d}}{\mathrm{d}t} \sum_k \frac{e^2 n}{T_i} \left\langle \Gamma_{0i}(b) |\delta\phi_k|^2 \right\rangle, \tag{4.12}$$

where $\Gamma_{0i}(b) = \mathrm{I}_0(b) \exp(-b)$ and $b = k_\perp^2 \rho_i^2$. If we now sum the contributions from the ions and the electrons, given by (4.12) and (4.11), after using quasineutrality, we arrive at

electrostatic energy balance,

$$\frac{\mathrm{d}}{\mathrm{d}t} \sum_{\boldsymbol{k}} E(\boldsymbol{k}, t) = 2 \sum_{\boldsymbol{k}} \left(\mathrm{K}_i(\boldsymbol{k}, t) + \mathrm{K}_e^{\mathrm{tr}}(\boldsymbol{k}, t) \right). \tag{4.13}$$

Here, $E(\boldsymbol{k}, t)$ is electrostatic energy contained in the potential fluctuations in this system given by

$$E(\boldsymbol{k}, t) = \frac{e^2 n}{T_i} \left[\left\langle (1 + \tau - \Gamma_{0i}(b)) |\delta\phi_{\boldsymbol{k}}|^2 \right\rangle - \frac{\tau}{2V} \sum_j \int_{1/B_{\min}}^{1/B_{\max}} \tau_{B,j} |\overline{\delta\phi}_{j,\boldsymbol{k}}|^2 \, \mathrm{d}\lambda \right], \tag{4.14}$$

where $\tau = T_i/T_e$. The drive terms $\mathrm{K}_i(\boldsymbol{k}, t)$ and $\mathrm{K}_e^{\mathrm{tr}}(\boldsymbol{k}, t)$ are the work performed by the ions and trapped electrons on the electric field, respectively, and are given by

$$\mathrm{K}_i(\boldsymbol{k}, t) = -\mathrm{Re} \left\langle e \int \delta\phi_{\boldsymbol{k}}^* \mathrm{J}_{0i} \left(v_\parallel \frac{\partial g_{i,\boldsymbol{k}}}{\partial l} + \mathrm{i}\omega_{\mathrm{di}} g_{i,\boldsymbol{k}} \right) \mathrm{d}^3 v \right\rangle, \tag{4.15}$$

and

$$\mathrm{K}_e^{\mathrm{tr}}(\boldsymbol{k}, t) = \mathrm{Re} \left\langle e \int \mathrm{i}\overline{\omega}_{\mathrm{de}} \delta\phi_{\boldsymbol{k}}^* g_{e,\boldsymbol{k}} \, \mathrm{d}^3 v \right\rangle. \tag{4.16}$$

The total electrostatic energy drive is then $K(\boldsymbol{k}, t) = \mathrm{K}_i(\boldsymbol{k}, t) + \mathrm{K}_e^{\mathrm{tr}}(\boldsymbol{k}, t)$. The drive, K, determines the rate at which the electrostatic energy of the system can grow, given the energy transfer possible by wave–particle interactions. This form of electrostatic energy balance is similar to forms derived by Helander *et al.* (2013) and Plunk *et al.* (2017), where they were concerned with normal modes.

4.3. *Generalised free energy*

Now that we have found forms for both the electrostatic energy and the Helmholtz free energy, we can construct the generalised free energy, as shown in Part 3, by considering the linear combination

$$\tilde{H} = H - \Delta E, \tag{4.17}$$

where Δ is a real constant. Here $\tilde{H}$ can be guaranteed to be a positive-definite energy norm if Δ is chosen correctly; for example, any negative real choice of Δ gives a positive definite energy measure. However, positive-definiteness will not be fulfilled beyond a certain magnitude of positive Δ. Note that $\tilde{H}$ does not define a single energetic norm, but rather an infinite set of norms for each allowable value of Δ, all of which are invariant under nonlinear interactions between different wavenumbers if Δ is chosen to be independent of k (Plunk & Helander 2023). The Helmholtz free energy is a special case in this set of energy norms for which $\Delta = 0$.

The energy balance equation for $\tilde{H}$ is

$$\frac{\mathrm{d}}{\mathrm{d}t} \sum_{\boldsymbol{k}} \tilde{H}(\boldsymbol{k}, t) = 2 \sum_{\boldsymbol{k}} \left(D(\boldsymbol{k}, t) - \Delta K(\boldsymbol{k}, t) \right). \tag{4.18}$$

This energy balance is now 'aware' of both the source of free energy growth (the gradients), and the mechanism by which it is extracted (wave–particle interactions). As

defined in Part 3, the instantaneous growth rate of the generalised free energy is

$$\Lambda = (D - \Delta K)/\tilde{H}. \tag{4.19}$$

Note that because $\tilde{H}$ defines a positive definite square norm, the linear, normal mode growth γ_L is bounded by the maximum possible value of Λ,

$$\gamma_L \leqslant \max_{g_e, g_i} \Lambda. \tag{4.20}$$

5. Optimal modes

We now seek the distribution functions g_i and g_e which extremise the value of Λ – the optimal modes. These optimal modes are found by varying (4.19) with respect to the distribution function for each species and seeking an extremum ($\delta \Lambda = 0$). This optimisation procedure yields two coupled variational problems, one for each species, given by

$$\Lambda \frac{\delta \tilde{H}}{\delta g_a} = \frac{\delta D}{\delta g_a} - \Lambda \frac{\delta K}{\delta g_a}. \tag{5.1}$$

However, when performing the variation, we must take into consideration that the electron distribution function is independent of the field-line-following coordinate l. To enforce this, when computing the variation of a functional $F[g_e]$ as

$$\frac{\delta F}{\delta g_e} = \left. \frac{\mathrm{d}}{\mathrm{d}\varepsilon} \right|_{\varepsilon=0} F[g_e + \varepsilon h_e], \tag{5.2}$$

the perturbation h_e is taken to be independent of l. To make the impact of l-independence clearer, we define the inner product on the space of trapped-electron distribution functions as

$$(g_e, g_e)_{\mathrm{tr}} = \frac{2\pi}{V} \sum_j \int_{1/B_{\max}}^{1/B_{\min}} \mathrm{d}\lambda \int_0^\infty \mathrm{d}v \, v^2 \tau_{B,j} T_e \frac{|g_e|^2}{F_{e0}}, \tag{5.3}$$

which can be derived from the inner product for ion distributions (which we also use for the ion distributions here) defined in Part 3,

$$(g_i, g_i) = \left\langle T_i \int \frac{|g_i|^2}{F_{i0}} \, \mathrm{d}^3 v \right\rangle \tag{5.4}$$

by expressing the velocity space integration in pitch-angle coordinates, under the assumptions of l-independence, and g_e being zero in the passing region of velocity space.

Evaluating the two variational problems (5.1) and expressing the result in terms of the inner products defined above, for the respective species over which the variation is performed, yields two coupled eigenvalue problems for the optimal modes and the growth rate Λ,

$$\Lambda \sum_b \tilde{\mathcal{H}}_{\mathrm{ab}} g_b = \sum_b \left(\mathcal{D}_{\mathrm{ab}} g_b - \Delta \mathcal{K}_{\mathrm{ab}} g_b \right), \tag{5.5}$$

where the operators $\tilde{\mathcal{H}}_{\mathrm{ab}}$, $\mathcal{D}_{\mathrm{ab}}$ and $\mathcal{K}_{\mathrm{ab}}$ are given in Appendix A. Here, and from now on, we will omit the subscript 'k' for simplicity. These operators are expressed in terms of a

finite set of velocity-space moments of the distributions,

$$\kappa_{1a} = \frac{1}{n} \int g_a \mathrm{J}_{0a} \, \mathrm{d}^3 v, \tag{5.6}$$

$$\kappa_{2a} = \frac{1}{n} \int \left(\frac{v^2}{v_{Ta}^2} \right) g_a \mathrm{J}_{0a} \, \mathrm{d}^3 v, \tag{5.7}$$

$$\kappa_{3e} = \frac{1}{n} \int \overline{f(l)(1 - \lambda B/2)} \left(\frac{v^2}{v_{Te}^2} \right) g_e \, \mathrm{d}^3 v, \tag{5.8}$$

$$\kappa_{3i} = \frac{1}{n} \int \left(\frac{v_\perp^2}{2 v_{Ti}^2} + \frac{v_\parallel^2}{v_{Ti}^2} \right) g_i \mathrm{J}_{0i} \, \mathrm{d}^3 v, \tag{5.9}$$

$$\kappa_{4i} = \frac{1}{n} \int \left(\frac{v_\parallel}{v_{Ti}} \right) g_i \mathrm{J}_{0i} \, \mathrm{d}^3 v, \tag{5.10}$$

$$\kappa_{5i} = \frac{1}{n} \int \left(\frac{v_\parallel}{v_{Ti}} \right) g_i \frac{\partial \mathrm{J}_{0i}}{\partial l} \, \mathrm{d}^3 v, \tag{5.11}$$

where we have written $\hat{\omega}_{\mathrm{de}}(l) = \tilde{\omega}_{\mathrm{de}} f(l)$, $f(l)$ is a dimensionless function which captures the l-dependence of $\hat{\omega}_{\mathrm{de}}$, and $\tilde{\omega}_{\mathrm{de}}$ is a constant with units of inverse time. Note that, due to the appearance of the bounce average in each of the electron operators in Appendix A, the equation which results from the variation of the electron distribution function gives an optimal g_e which is independent of l as required.

This eigenvalue problem for the optimal mode growth has 'full' dependence on the magnetic geometry of the flux tube, i.e. the magnetic field strength, the curvature and the metric coefficients, all as a function of l. The system can be closed exactly in terms of the moments κ_{na} by taking moments of the two equations given by (5.5). This results in an 8×8 system of integrodifferential equations which must be solved for the eigenvalue Λ.

This system of equations can be solved for any choice of Δ, for which $\tilde{H}$ is positive definite, allowing us to compute the optimal mode growth rate for any element in the set of energy norms defined by $\tilde{H}$. Thus, for a given scenario (e.g. plasma parameters and geometry), we can seek the value of Δ which corresponds to the most restrictive norm on the dynamics of the system within this set. This will give the tightest possible bound on linear instability growth in accordance with (4.20).

In practical terms, this means that for each scenario we can optimise over Δ to find the tightest upper bound on instability growth in the system. Here, this optimisation will be carried out numerically. As explained in Part 3, this tightest upper bound is guaranteed to be less than (or equal to) that of the Helmholtz free energy at $\Delta = 0$ and the magnitude of the optimal Δ can be thought of as the relative importance of wave–particle effects in restricting the optimal growth for a given scenario.

Note that, due to the complexity of the system in general magnetic geometry, we are unable to derive generally the limiting value of Δ beyond which positive definiteness is no longer guaranteed. However, this does not pose a problem when solving the system numerically as positive definiteness can be checked at each step when optimising over Δ.

6. Solving the system in the slow-ion-transit limit

To make finding the solution to the eigenvalue problem more straightforward, we consider the limit $L/v_{Ti} \gg \tau_D$, where the ion transit time is much longer than the typical instability time scale. In this limit, we can neglect the derivatives along the magnetic field

line that arise due to the parallel ion motion. This reduces the dimensionality of the system by removing κ_{4i} and κ_{5i} from the problem, leaving a 6×6 system of integroalgebraic equations. Note that this ordering is the typical 'toroidal' ITG and TEM ordering often applied in linear, normal-mode analyses (Biglari, Diamond & Rosenbluth 1989; Helander *et al.* 2013; Plunk *et al.* 2017). The system of moment equations in this limit is given in Appendix B.

6.1. *A square magnetic well*

We cannot make much progress towards an analytical solution of this system for a general magnetic geometry. Thus, to gain some insight into the behaviour of the system, we consider a 'square' magnetic field of the form

$$
B(l) = \begin{cases} B_{\min}, & -L/2 < l < L/2, \\ B_{\max}, & |l| \geqslant L/2, \end{cases} \tag{6.1}
$$

with $\omega_{\mathrm{da}}(l) = \mathrm{const.}$ and $k_\perp = \mathrm{const.}$ In this simplified geometry, the κ_{na} eigenfunctions are constant inside the magnetic well between $-L/2 < l < L/2$ and the κ_{ne} moments must vanish for $|l| \geqslant L/2$. In this case, there are two possibilities, either the ion moments must also vanish in this region, or the electron moments are zero everywhere, corresponding to the system with adiabatic electrons. Both of these solutions are realisable, with the adiabatic electron solution being described in Part 3. Here, we concern ourselves with the eigenfunctions that vanish at $B_{\max}$, whilst keeping in mind that the adiabatic electron solution is also present in the system outside the well.

The solution to the eigenvalue problem in this square magnetic geometry is given in appendix C and is denoted as Λ_{SW}. We find that the value of Δ beyond which the system is not guaranteed to be Hermitian (i.e. implying a violation of positive-definiteness) is

$$
\Delta < \frac{1+\tau}{\Gamma_0 + \tau\varepsilon}, \tag{6.2}
$$

where $\varepsilon = \sqrt{1 - B_{\min}/B_{\max}}$. While we will mostly employ this solution as a benchmark for comparison with numerical solutions, it can provide some insight into the behaviour of the optimal mode system in this limit. Firstly, in the Helmholtz limit with $\Delta = 0$, we see that Λ_{SW} reduces to an expression of the same form as the fully kinetic electron Helmholtz bound derived in Appendix D of Part 2, with the only difference being the lack of finite-electron-Larmor-radius effects in the solution here, and the reduction of the size of the electron response by the trapped-particle fraction ε. Later, we will see that this reduction of the population of electrons which contributes to instability growth has a profound impact on the qualitative behaviour of the bound. Moreover, in the limit of $\varepsilon \to 0$, we recover the adiabatic electron Helmholtz bound of Part 1. Thus, the system studied here behaves like an intermediate limit between the fully kinetic and adiabatic electron limits.

For the generalised free energy case, with $\Delta \neq 0$, we also note that, in the limit of $\varepsilon \to 0$, Λ_{SW} reduces to the adiabatic electron result of Part 3 in the toroidal ITG limit.

6.2. *Numerically solving the system*

The analytical solution in the square well, Λ_{SW}, already provides some insight into the behaviour of the eigenvalue problem but does not capture the subtleties of the bounce-averaged electron response. In realistic magnetic geometries, the local curvature along the field line may differ vastly from the bounce-averaged curvature felt by trapped

electrons due to the variation of the magnetic field strength along the field line. As a result, the ions and electrons in the bounce-averaged limit can experience drifts which are vastly different. This could be captured in the square well geometry by stipulating that the ions and electrons experience different curvatures in the well, but this would be a coarse approximation of the realistic situation.

To get a better sense of the behaviour of the system in more realistic geometries, we resort to numerically solving the system of integroalgebraic equations given by the moment form of the kinetic eigenvalue problem (5.5) in the slow-ion-transit limit ($L/v_{\mathrm{Ti}} \gg \tau_D$). For the sake of simplicity, we do this in simple, toy-model magnetic fields. Here, we discretise the system on a basis of cosines in l, with zeros at the maximum of magnetic field strength (the eigenfunctions of interest are purely even in a symmetric geometry, and must vanish at $B = B_{\max}$), and use a recently developed numerical package to evaluate the bounce averages and integrals over λ (Mackenbach *et al.* 2023*a*).

7. Helmholtz free energy ($\Delta = 0$) bounds

For the case of $\Delta = 0$, the generalised free energy reduces to the Helmholtz free energy, and the κ_{3a} moments do not contribute to the system of equations. This reduces the dimensionality of the system to 4×4. In this limit, the optimal modes do not depend on magnetic curvature, but retain dependency on $B(l)$ and the variation of $k_\perp$ with l. We will refer to the optimal mode growth rate of this system with $\Delta = 0$ as the Helmholtz bound. To get a sense of how the optimal modes behave in response to the presence of different plasma gradients, we consider three cases: the case of a pure ion-temperature gradient in the plasma ($\nabla n = 0$, $\nabla T_e = 0$) that we refer to as the 'pure ITG case'; a pure density gradient ($\nabla T_i = 0$, $\nabla T_e = 0$) case that we refer to as the 'pure TEM case'; and a case with only an electron temperature gradient ($\nabla n = 0$, $\nabla T_i = 0$ which we refer to as the 'pure ETG-TEM case'. While we have only considered single gradients here for simplicity, we note that the optimal modes can equally be applied to mixed gradient cases.

In figure 1, we show the Helmholtz bound of the system as a function of $b_i = k_\perp^2 \rho_i^2$. Here, for the numerical solution, we consider a magnetic field of the form $B(l) = B_0 - B_1 \cos(l)$ with $B_0 = 1$ and $B_1 = 0.2$, and use $k_\perp = $ const. for simplicity. In a sinusoidal field such as this, the magnetic trapping wells are identical and are separated by identical maxima (like in an omnigenous field), thus we need only solve the system in a single well with $-\pi \leqslant l \leqslant \pi$. Note that numerically solving the integroalgebraic system results in a spectrum of eigenvalues (an example of which can be seen in figure 2), which are all real due to the Hermiticy of the system, and come in pairs of positive and negative values of equal magnitude due to the time reversibility of the system (Plunk & Helander 2022). In figure 1 we only show the fastest-growing optimal mode growth rate (the largest positive eigenvalue) for clarity.

We also show the analytical Helmholtz bound of the system in a square magnetic trapping well of the same depth, Λ_{SW}, given by (C18) with $\Delta = 0$. We compare these Helmholtz bounds with the bounce-averaged trapped electron response to the Helmholtz bounds with adiabatic electrons, given by (6.20) in Helander & Plunk (2022), and the Helmholtz bound with fully kinetic electrons, taken from Appendix C of Plunk & Helander (2022). For all gradients considered, we find that the numerical solution in the sinusoidal magnetic field closely follows the analytical solution for the square magnetic trapping well.

For the pure ITG case (figure 1*a*), we find that the Helmholtz bound of the system with the bounce-averaged trapped electron response lies between the bounds for the adiabatic and fully kinetic electron systems. Moreover, in figure 2 we see that this is true of the entire spectrum of solutions, which appear to be bounded from below in magnitude by the adiabatic electron bound. We note that, for all gradients, the optimal mode growth
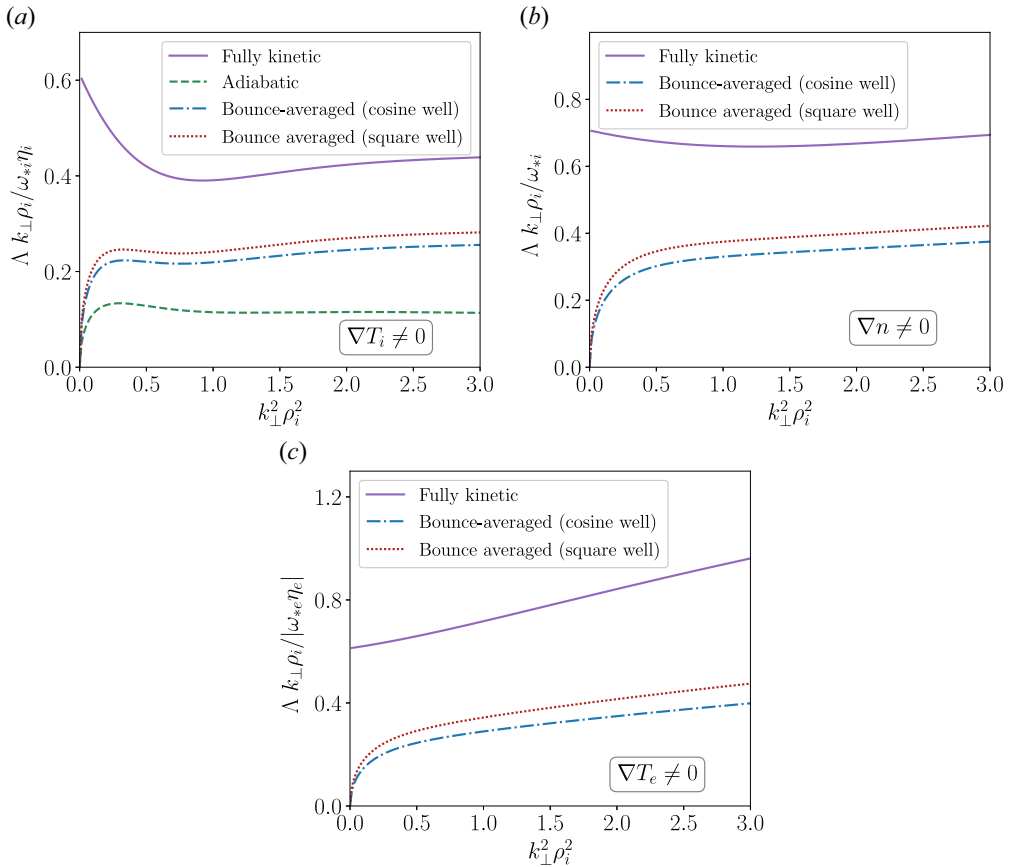
(a)

(b)

(c)

FIGURE 1. Optimal mode growth rates Λ of the Helmholtz free energy with $\tau = 1$ as a function of $k_\perp^2 \rho_i^2$ for the various electron models. Panel (a) shows the pure ITG case, (b) shows the pure TEM case and (c) shows the pure ETG-TEM case.
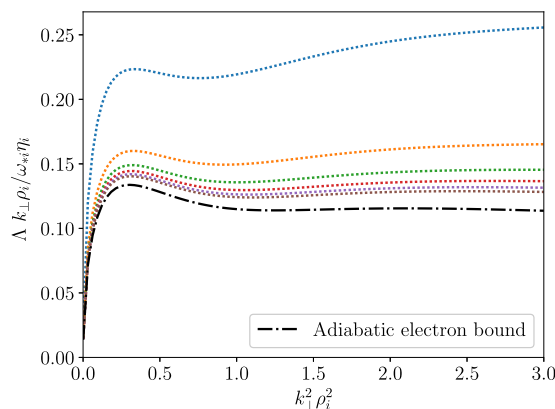

FIGURE 2. Spectrum of numerical solutions to the kinetic eigenvalue problem (5.5) for a sinusoidal magnetic field strength with $\tau = 1$ for the pure-ITG case alongside the adiabatic electron optimal growth rate. Shown are the six largest eigenvalues found numerically.
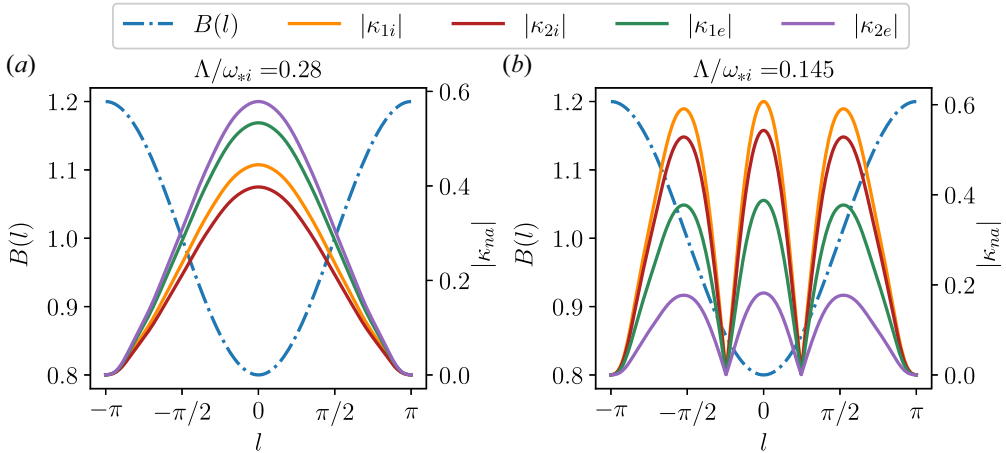
FIGURE 3. Eigenfunctions of the kinetic eigenvalue problem (5.5), obtained numerically, for $\Delta = 0$ (Helmholtz limit of the generalised free energy) with $\tau = 1$, $b_i = 1.5$, in the pure TEM case. Here, the absolute values of the κ_{na} moments are shown as a function of l, alongside the magnetic field strength $B(l)$, for the eigenfunction with the largest eigenvalue (*a*) and the second largest (*b*).

rate tends to zero as $k_\perp \to 0$ in the bounce-averaged system. This signifies the removal of the 'magnetohydrodynamic-like' instability mechanism present in the fully kinetic electron Helmholtz bound, which causes the bound to approach a finite value in this limit. Mathematically, the cause of this difference is illustrated by the square well solution Λ_{SW} where as $k_\perp \to 0$, the numerator tends to zero and the denominator is proportional to $(1 - \varepsilon)$, which is finite unless the trapped particle fraction is unity. Thus, we have $\Lambda_{SW} \to 0$ as $k_\perp \to 0$. This is in contrast to the fully kinetic electron bound of Part 2, whose denominator goes to zero in the limit $k_\perp \to 0$ in such a way that the bound remains finite. Physically, the Helmholtz bound with fully kinetic electrons overestimates the degree of instability because it contains a contribution from non-adiabatic passing electrons which, in toroidal geometry, does not contribute on time scales longer than the electron transit time.

The bounce-averaged electron system also yields a Helmholtz bound for the pure TEM case and the pure ETG-TEM case; see figures 1(*b*) and 1(*c*). In this bounce-averaged electron system, this provides a bound on the growth of ∇n and ∇T_e-driven TEMs (this does not extend to 'true' ETGs, which exist at larger values of $k_\perp$ thus violating our assumption of $k_\perp \rho_e \ll 1$ and require a non-adiabatic passing electron response).

In figure 3, an example of two of the fastest-growing eigenmodes is shown for the pure TEM case. The eigenfunctions are similar (in l-variation) to the expectation from the linear theory, with the fastest growing mode having a maximum where the largest fraction of trapped electrons reside at the minimum of the magnetic field strength. The fastest-growing eigenmode has a significant contribution from the κ_{ne} moments, indicating their importance for extracting free energy at these parameters.

8. Generalised free energy bounds

We now turn our attention to the general problem in which Δ is a free parameter. For this case where $\Delta \neq 0$, the species moments κ_{3a}, are retained. Thus, the optimal modes of this system depend on the magnetic curvature drift, ω_{da}, for each species. We seek values of Δ which minimise the maximum growth rate Λ of the generalised free energy, giving the
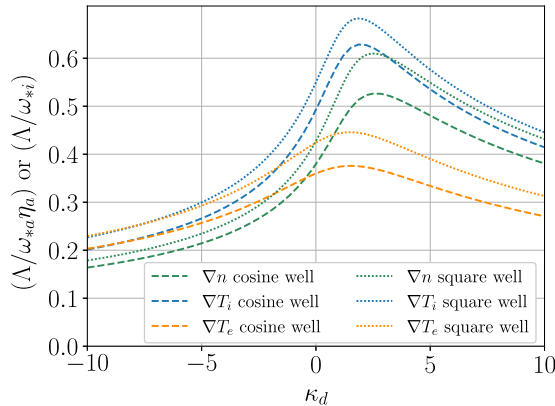
FIGURE 4. The optimal mode growth rate of generalised free energy, at the minimising value of Δ, versus the drive parameter κ_d at $\tau = 1$. The analytical square well with constant curvature solution is shown alongside the numerical solutions of the eigenvalue problem in a cosine magnetic well with constant curvature. These are computed for a density-gradient-driven case (pure TEM case), an ion-temperature-gradient-driven case (pure ITG case) and an electron-temperature-gradient-driven case (pure ETG-TEM case).

lowest possible upper bound. The largest resulting optimal growth rate, at this minimising value of Δ, gives an upper bound on instabilities, in the considered limit, that depends on the magnetic curvature.

Because of the complexity of the general system, we perform the optimisation over Δ numerically and exclude values for which positive definiteness is violated. However, we have found that the optimisation space of $\Lambda(\Delta)$ is very smooth and that a global minimum is easily found.

As a first test for the numerical solution, to facilitate comparison with the analytical solution for square magnetic trapping well with constant curvature, we solve the system numerically for the case of a magnetic field of the form $B(l) = B_0 - B_1 \cos(l)$ with $B_0 = 1$ and $B_1 = 0.1$ with constant curvature, $\hat{\omega}_{\mathrm{da}}(l) = \mathrm{const}$. Following the analysis of the generalised free energy with adiabatic electrons of Part 3, we consider the instability drive parameter $\kappa_d = \omega_{*i}/\hat{\omega}_{\mathrm{di}}$ or ($\kappa_d = \omega_{*i}\eta_i/\hat{\omega}_{\mathrm{di}}$ for the pure ITG case and $\kappa_d = |\omega_{*e}\eta_e|/\hat{\omega}_{\mathrm{di}}$ for the pure ETG-TEM case). We thus have $\hat{\omega}_{\mathrm{da}}/\omega_{*i} = \mathrm{sign}(e_a)\kappa_d^{-1}T_a/T_i$ for each species. Under this normalisation, if $\kappa_d > 0$, then $\hat{\omega}_{\mathrm{da}}\omega_{*a} > 0$ for both species, corresponding to 'bad' curvature where linear instability is expected. The case of $\kappa_d < 0$ corresponds to 'good' curvature, where the system is expected to be linearly stable.

In figure 4, we show the optimal mode growth for the pure TEM case, the pure ETG-TEM case, and for the pure ITG case, as the curvature-drive parameter κ_d is varied. We see that the square and the cosine trapping wells follow similar trends with κ_d, attaining a maximum for a finite positive value of κ_d, where the optimal bound is obtained for $\Delta = 0$ and therefore coincides with the Helmholtz bound. This feature of the generalised free energy bound overlapping with the Helmholtz bound at a particular value of the curvature drive was also found for the adiabatic electron analysis in Part 3. The optimal bound decreases monotonically away from this maximum towards the 'strongly driven' limit of large positive κ_d and in the direction of small κ_d in the 'resonant limit'. The bound also decreases for $\kappa_d \lesssim 0$ where the curvature is favourable ('good').

In figure 5, we compare the optimal mode growth in the square well, Λ_{SW}, with constant curvature to the solution to the linear dispersion relation with bounce-averaged electrons
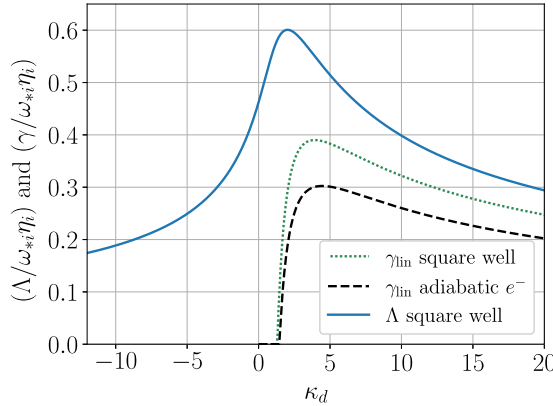
FIGURE 5. Comparison between the generalised upper bound Λ_{SW}, and the linear growth rate, for a pure ITG case in a square magnetic well with $B_{\min}/B_{\max} = 0.1$, $\tau = 1$, and constant curvature (see Appendix D). Here, the drift-kinetic limit has been considered for simplicity ($\mathrm{J}_{0i} \approx 1$).

(details given in appendix D) in the same geometry, in the pure ITG case. Once again, we vary the drive parameter κ_d to compare how each solution depends on the curvature inside the well. We confirm that the linear result lies below the upper bound, and we find that, much like the behaviour of the upper bound, the presence of bounce-averaged electrons in the linear dispersion relation 'lifts up' the linear growth rate of the ITG. In regions where the normal modes are stable, the optimal modes have a finite but reduced growth rate, as was found in Part 3 for the adiabatic electron system.

8.1. *Impact of the maximum-J property*

A class of magnetic configurations in which the gyrokinetic system with bounce-averaged electrons is particularly interesting is provided by so-called 'maximum-J' geometries, where the radial profile of the parallel adiabatic invariant,

$$J(v, \lambda, \psi, \alpha) = m_e v \int_{l_1}^{l_2} \sqrt{1 - \lambda B} \, \mathrm{d}l, \qquad (8.1)$$

has a maximum at the magnetic axis, and decreases radially (Rosenbluth 1968). In such geometries, the electrons experience good curvature everywhere because

$$\omega_{*e} \overline{\omega}_{\mathrm{de}} = -\frac{T_e k_\alpha^2}{e^2 \tau_B} \frac{\mathrm{d} \ln n}{\mathrm{d}\psi} \frac{\partial J}{\partial \psi} \qquad (8.2)$$

is negative for all trapped electrons if $\partial J/\partial \psi < 0$ and $\mathrm{d} \ln n/\mathrm{d}\psi < 0$, as is usually the case in fusion plasmas (Proll *et al.* 2012; Helander *et al.* 2013). Quasi-isodynamic stellarators are a particular type of optimised stellarator (Helander & Nührenberg 2009; Nührenberg 2010) which can be designed to have this property (Sánchez *et al.* 2023; Rodríguez, Helander & Goodman 2024). In such devices, the local curvature (as seen by the ions) may be unfavourable, but the bounce-averaged curvature for trapped electrons is always favourable. Many results from normal-mode theory, as well as gyrokinetic simulations, have found that the trapped electron population in these geometries have a stabilising influence if a plasma density gradient is present (Proll *et al.* 2012; Plunk *et al.* 2014; Alcusón *et al.* 2020; Proll *et al.* 2022). The physical reason for this enhanced stability
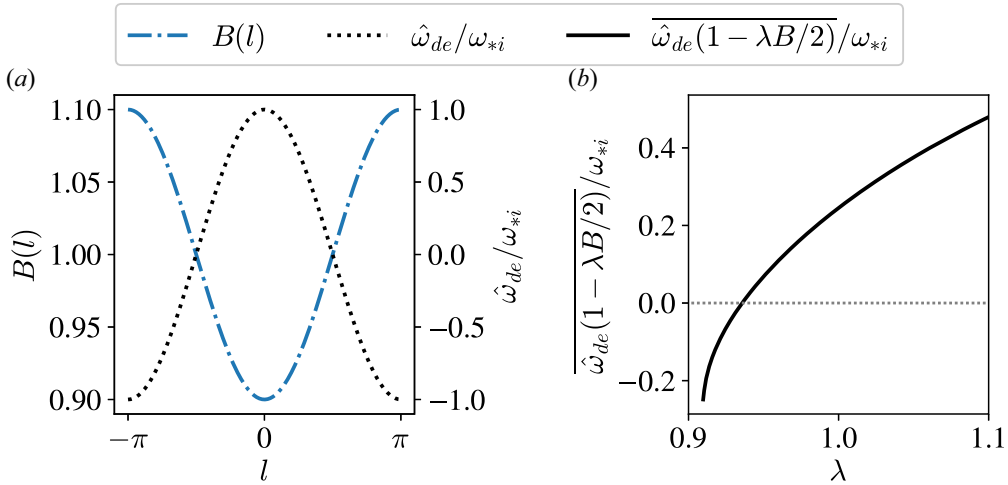
FIGURE 6. An example of an approximately maximum-J toy geometry, where most trapped electrons, particularly those that are deeply trapped, experience bounce-averaged good curvature. (*a*) The curvature is shown alongside the magnetic field strength, where negative values indicate bad curvature. (*b*) The λ-dependence of the bounce-averaged electron drift is shown.

can be traced back to the fact that relatively little of the thermal energy is 'available' for conversion to instabilities (Helander 2017; Mackenbach *et al.* 2023*b*).

To investigate if this property is present in the optimal mode system, we require a test geometry where the ions may experience bad curvature locally, while the bounce-averaged curvature of the electrons can be independently varied. A simple model magnetic geometry can be seen in figure 6. In this geometry, we choose a curvature of the form $\hat{\omega}_{da}(l)/\omega_{*i} = \text{sign}(e_a)\sigma_d \cos(l)T_a/T_i$ and $B(l) = B_0 + B_1 \cos(l)$, where once again, we take $B_0 = 1.0$ and $B_1 = 0.1$. In this toy geometry, σ_d is a parameter which determines the relative magnitude of the gradient length scale and the maximum radius of curvature, similar to the familiar R/L_n or R/L_{T_a} normalisation, where R is the major radius of the torus and L_{n,T_i} is the scale length of the density or temperature gradients, respectively. With this model geometry, by changing the sign of σ_d we can choose between a mostly maximum-J geometry for $\sigma_d < 0$, where most trapped electrons, particularly those which are deeply trapped, experience bounce-averaged good curvature, and a mostly minimum-J geometry for $\sigma_d > 0$. Importantly, we can make this change between maximum-J and minimum-J geometry without changing the field-line-average curvature (zero in this case), whilst always having a region of unfavourable curvature along the field line.

In figure 7, we show the optimal growth rate Λ as σ_d is varied, the pure ITG case, pure TEM case and pure ETG-TEM case. The upper bound in the pure TEM case is lower in the maximum-J geometries (negative σ_d) than in the equivalent minimum-J geometries (positive σ_d). To explore the physical mechanism at play, we also test the dependence of the optimal mode growth on the curvature drift for each species separately. For $\sigma_d < 0$ (maximum-J), removing the electron drift frequency (the instability mechanism that remains is analogous to the ITEM of Plunk *et al.* (2017)) increases growth rates if $|\sigma_d|$ is small, and has little effect for σ_d large and negative. Thus, $\overline{\omega}_{de}$ has a stabilising effect in the maximum-J geometries, in agreement with the expectation linear theory. Moreover, in maximum-J geometries at large negative values of σ_d, the instability mechanism is largely
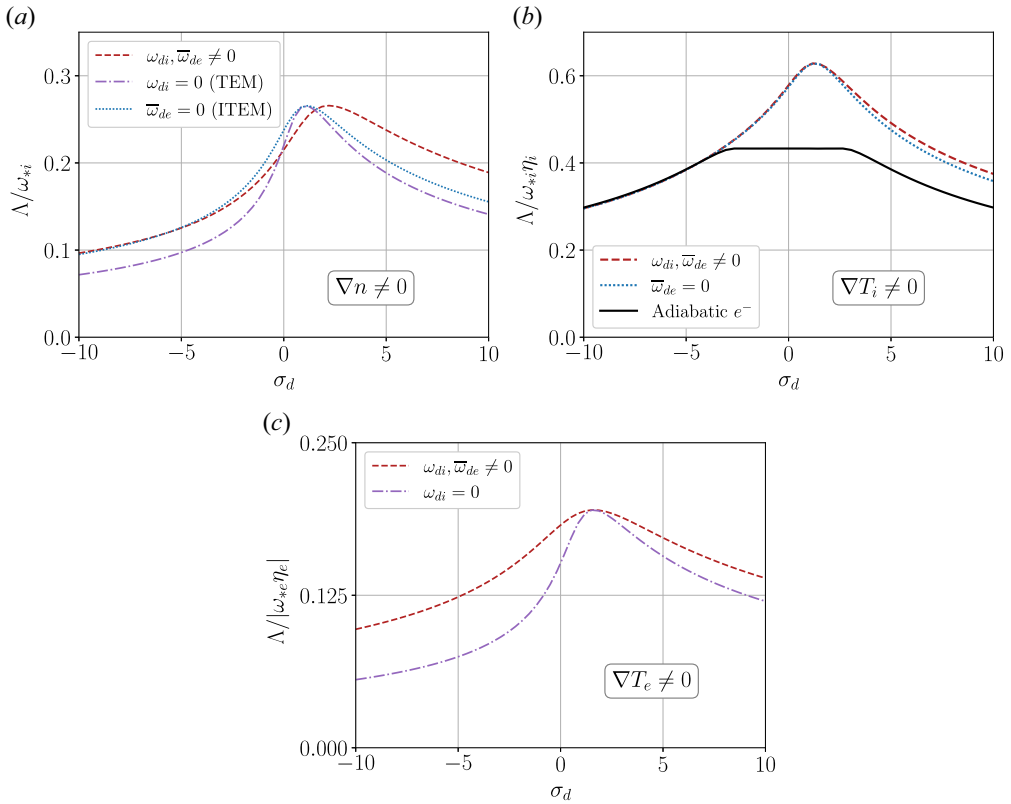
FIGURE 7. The optimal mode growth rate of generalised free energy, for the minimising Δ, versus the drive parameter σ_d. Negative and positive values of this parameter correspond to the 'maximum-J' and 'minimum-J' cases of the model geometry shown in figure 6. (*a*) The pure TEM case is shown at $k_\perp \rho_i = 1.5$, (*b*) the pure ITG case in the drift kinetic limit ($J_{0i} \approx 1$) is shown and (*c*) shows the pure ETG-TEM case at $k_\perp \rho_i = 1.5$. The impact of species-dependent curvature drifts on each case is explored by zeroing out $\hat{\omega}_{\mathrm{di}}$ or $\overline{\omega}_{\mathrm{de}}$ independently.

reliant on the ion curvature drift, as is expected from the linear ITEM or ubiquitous mode (Coppi & Pegoraro 1977).

For $\sigma_d > 0$ (minimum-J), the removal of the curvature drift for either species in the pure TEM case serves to move the maximum value of the optimal growth rate towards lower values of σ_d and greatly reduces the growth rate for large σ_d. This suggests that the drifts of both species are important for the optimal extraction of free energy from the gradients.

In the pure ETG-TEM case, we see a reduction of the optimal mode growth for $\sigma_d <$ 0. This is in keeping with the expectation from the dispersion relation of Plunk *et al.* (2017), which shows that the maximum-J property, associated with the relative direction of the bounce-averaged drift to the electron diamagnetic frequency, also exerts a stabilising influence in the strongly driven limit when η_e is finite. The optimal mode analysis here suggests that this benefit extends into the resonant limit (small σ_d).

We observe that maximum-J configurations also exhibit lower optimal growth in the ITG scenario ($\nabla n = 0$, $\nabla T_e = 0$). This is despite the absence of any electron free energy source, something which has not been predicted previously from linear normal-mode theory. It is found that beyond a negative value of σ_d of sufficient magnitude, the ITG upper bound with bounce-averaged electrons coincides with that of the adiabatic electron upper

bound of Part 3 computed in this geometry (because the bound with adiabatic electrons is local in this limit, here we evaluate the bound at each point in l in the toy geometry and plot the largest value found). This is also reflected in the eigenfunction (not shown), which tends towards a delta function at the location of maximum magnetic field strength, where the trapped electron contribution is zero, suggesting that the adiabatic ITG solution to (5.5) becomes the solution with the largest Λ for these values of σ_d. As shown in figure 7, this mechanism of stabilisation in maximum-J geometry is present even if $\overline{\omega}_{de} = 0$. Thus, this stabilising mechanism in maximum-J geometries is distinct from the known mechanism that follows from the difference in sign between $\overline{\omega}_{de}$ and ω_{*e}^T (Proll *et al.* 2022).

8.1.1. *Interpreting with linear theory*

To interpret the observed reduction of the ITG-driven optimal mode growth in maximum-J geometries without a source of electron free energy, we turn to expressions from linear normal-mode theory (i.e solutions to the gyokinetic equation which evolve in time like $\exp(-i\omega t)$, where ω is the complex frequency). The comparable linear dispersion relation is given by (3.5) in Plunk *et al.* (2017), for the case of a pure ITG, which is valid if the mode frequency satisfies $\omega/(\omega_{*i}\eta_i) \sim (\omega_{di}/\omega_{*i}\eta_i)^{1/2} \ll 1$ (i.e. in the regime of large κ_d). Taking the drift-kinetic limit ($J_{0i} \approx 1$), the normal mode frequency is given by

$$\omega = \pm\sqrt{-\omega_{*i}\eta_i \int_{-\infty}^{+\infty} \hat{\omega}_{di}(l)|\delta\phi|^2 \frac{dl}{B}} \Bigg/$$
$$\left(\tau \int_{-\infty}^{+\infty} |\delta\phi|^2 \frac{dl}{B} - \frac{\tau}{2} \sum_j \int_{1/B_{\max}}^{1/B_{\min}} \tau_{B,j}|\overline{\delta\phi}_j|^2 \, d\lambda\right)^{1/2}, \tag{8.3}$$

where instability growth is given by a positive imaginary part of ω which arises due to regions of bad curvature along the magnetic field ($\omega_{*i}\eta_i\hat{\omega}_{di} > 0$). We see that when the ITG is unstable, the trapped electron contribution in the denominator acts to further destabilise the mode by making the denominator (which is always positive (Helander *et al.* 2013)) smaller. This destabilising effect is due to the depletion of the Boltzmann response by the population of non-adiabatic trapped electrons.

The effect of the maximum-J property on this dispersion relation is most easily illustrated when the case of the 'square well' magnetic field with constant curvature inside the well is considered. Inside the well, the ITG frequency becomes $\omega = \pm\sqrt{-\omega_{*i}\eta_i\hat{\omega}_{di}/(\tau(1-\varepsilon))}$, where ε is the trapped particle fraction, and outside the well it is given by $\omega = \pm\sqrt{-\omega_{*i}\eta_i\hat{\omega}_{di}/\tau}$. If we consider a series of these square magnetic trapping wells with minima of $B = B_{\min}$ separated by regions of $B = B_{\max}$, with a magnetic curvature that alternates sign (from 'good' curvature to 'bad' curvature) between regions of $B = B_{\max}$ and $B = B_{\min}$, then there are two possibilities: either the bad curvature is located at the minimum of magnetic field strength, corresponding to a minimum-J geometry; or the bad curvature is located outside the well, corresponding to a maximum-J geometry.

In the minimum-J case, the ITG is unstable inside the well, with a growth rate given by $\omega = \pm\sqrt{-\omega_{*i}\eta_i\hat{\omega}_{di}/(\tau(1-\varepsilon))}$. In this scenario, the non-adiabatic population of trapped electrons can raise the ITG growth rate by depleting the Boltzmann response. On the other hand, in the maximum-J case, the ITG is stable inside the well because the curvature is favourable there ($\hat{\omega}_{di}\omega_{*i}\eta_i > 0$). Instead, the unstable ITG is outside of the well at $B = B_{\max}$ and the growth rate is $\omega = \pm\sqrt{-\omega_{*i}\eta_i\hat{\omega}_{di}/\tau}$, corresponding to the ITG growth rate if the electrons are treated adiabatically.

This behaviour can also be inferred from the ITG growth rate in general geometry (8.3), in which it can be seen that for instability to occur, the average of $\omega_{*i}\eta_i\hat{\omega}_{di}|\delta\phi|^2$ along the magnetic field line must be positive, such that $\delta\phi$ must have large amplitude in the regions of bad curvature. In maximum-J geometry, the regions of bad curvature are at different locations in l than the minima of magnetic field strength. In these geometries, for the instability criterion to be fulfilled, the non-adiabatic electron response, which is proportional to the average potential seen by the trapped electrons as they bounce in the magnetic well, will be necessarily small. Otherwise, if the electron contribution were large, the potential would have a large amplitude in a region of favourable curvature, thus impacting the instability criterion. As a result, the destabilising impact of trapped electrons on the ITG is diminished in such geometries.

This is not the case in minimum-J geometries, where the regions of bad curvature are located at the minima of B along the field line. In these geometries, the instability criterion and the magnitude of the trapped electron contribution are not in conflict, thus the ITG growth can be increased by the trapped electron population without impacting the instability mechanism.

In the optimal mode analysis, this effect is slightly obscured due to the optimisation over the Δ parameter, but the same basic behaviour can be observed in the expression for $E(\boldsymbol{k},t)$ given by (4.14), which is of the same form as the denominator in (8.3). Thus, the magnitude of $E(\boldsymbol{k},t)$ affects the magnitude of Λ via the denominator of (4.19), for non-zero values of Δ. This stabilising effect of maximum-J can be seen in figure 7, where for the ITG scenario, the upper bound with bounce averaged electrons approaches the adiabatic electron result for large negative values of σ_d, corresponding to an approximately maximum-J geometry.

To summarise this section, the impact of the trapped electron response on ITG instability in the absence of electron free energy is always destabilising, but the amount of destabilisation is impacted by the location of the most deeply trapped particles relative to the regions of bad curvature. To use a term coined in the literature for zonal-flows (Diamond *et al.* 2005), the location of the trapped particles changes the inertia of the ITG mode, with ITGs possessing lower inertia in minimum-J configurations than in those which are maximum-J. This may go some way towards explaining why simulations performed in newly optimised, highly maximum-J stellarators (Goodman *et al.* 2024) show a smaller increase in ITG-driven heat fluxes with the addition of kinetic electrons in comparison with configurations which do not satisfy the maximum-J property to the same degree.

9. Conclusion

We have studied the optimal modes of the generalised free energy for the case of a two-species system with fully gyrokinetic ions and bounce-averaged electrons. The central result of this effort is a system of integrodifferential equations (B1)–(B3) and (B10)–(B12), the solutions to which provide an upper bound on the possible instantaneous growth of any instabilities which satisfy $L/v_{\text{Te}} \ll \tau_D$. These bounds depend explicitly on the magnetic field strength of the chosen flux tube. Despite being more difficult to solve than the optimal mode systems of Parts 1–3 (requiring a numerical treatment for all but the simplest of magnetic fields), the eigenvalue problem here, which involves a relatively small number of velocity space moments of the distribution function, is still much simpler than the equivalent normal mode problem, which involves computing the full distribution function as a function of velocity space.

As is discussed in Parts 1–3, the upper bounds given by the fastest growing optimal modes not only give an upper bound on linear instability, but also have

nonlinear implications. This is because the nonlinear growth of the system is bounded by the growth of the fastest growing optimal mode. Here, however, the removal of the 'finite-electron-Larmor-radius' effects associated with retaining $k_\perp \rho_e$ results in an unbounded growth of Λ as $k_\perp \to \infty$. As a result, the nonlinear growth is also unbounded if all values of $k_\perp$ are considered. Thus, when seeking a bound on nonlinear growth, the spectrum in $k_\perp$ must be cut off at a chosen value, limiting its applicability to cases in which only the ion-scale dynamics are of interest, as is often done in gyrokinetic simulations. Other nonlinear implications of optimal modes also discussed in Part 2, such as their required presence in statistically steady turbulence (DelSole 2004; Landreman *et al.* 2015), also hold true for the optimal modes studied here.

The upper bounds computed here are specific to toroidal geometries with non-periodic flux tubes (i.e. tokamaks and stellarators) and as such, the Helmholtz bound we find behaves as expected in these geometries at small values of $k_\perp \rho_i$. This is in contrast to the fully kinetic electron Helmholtz bound of Part 2 which, in its generality, must also bound growth in closed-field-line geometries. The Helmholtz bounds of the bounce-averaged system are significantly lower than the Part 2 result for all gradients, as long as $k_\perp \rho_e \ll 1$.

Moreover, the generalised bound, which is optimised over the free parameter Δ, depends explicitly on all the geometry quantities associated with the flux-tube domain. Here, we neglected parallel ion motion in our system of equations for the sake of simplicity, focusing on the typical toroidal ITG-TEM limits familiar from normal-mode theory. We have found that the optimal modes exhibit much of the behaviour expected from normal modes, attaining a maximum growth rate (relative to the strength of the plasma gradients) when the curvature drift for both species is unfavourable and when the ratios of the diamagnetic frequencies and drift frequencies are close to unity. We have also demonstrated that the beneficial properties of maximum-*J* configurations expected from normal-mode theory are also captured by the optimal modes. This was also found to be the case for another measure of turbulent transport that is valid nonlinearly, the available energy of trapped electrons (Helander 2017; Mackenbach *et al.* 2023*b*).

An unexpected consequence of this work was the observation of reduced ITG mode growth rates in maximum-*J* configurations in comparison with a similar minimum-*J* configuration when trapped electrons are included, even in the absence of a source of free energy in the electron equation. This effect, observed in both the optimal modes and the normal modes, was found to be related to the 'inertia' of the ITG mode, which is larger in maximum-*J* devices.

The optimal modes presented in this work could form the basis of a 'target function' for stellarator optimisation, given that they depend explicitly on the magnetic geometry and plasma parameters. The optimal modes studied here exhibit the effects present in the adiabatic electron optimal modes of Part 3. In particular, the two-species upper bound here shows a reduction of instability in both the 'strongly driven' and 'resonant' limits of the drive parameter κ_d (or σ_d); these limits are also visible in the available energy analysis of Mackenbach *et al.* (2023*b*). This suggests that, for fixed plasma gradients, one could choose to reduce the amount of bad curvature experienced by both species thus increasing κ_d (or σ_d). Alternatively, in so-called 'critical-gradient optimisation', the amount of bad curvature could be increased (decreasing κ_d into the resonant limit), as performed by Roberg-Clark *et al.* (2023) for ITG-driven turbulence with adiabatic electrons. Our findings suggest that both strategies are viable for reducing the growth of instabilities including the response of trapped electrons. Moreover, as we have seen, these optimal modes capture the interaction of several physical effects associated with the maximum-*J* property and thus may directly inform the optimisation of the benefits of this

property in a way that is not captured by present maximum-J targets, which are generally not designed with turbulence in mind.

Acknowledgements

Editor P. Catto thanks the referees for their advice in evaluating this article.

Funding

Declaration of interests

The authors report no conflict of interest.

Appendix A. Determining the Hermitian linear operators

The Hermitian linear operators in (5.5) can be identified from the variational problem (5.1). To make the variation of $\tilde{H}$ more straightforward we invert the identity (4.7) to arrive at

$$
\tilde{H} = \left\langle T_e \int \frac{|g_e|^2}{F_{e0}} \, \mathrm{d}^3 v + T_i \int \frac{|g_i|^2}{F_{i0}} \, \mathrm{d}^3 v \right.
$$
$$
\left. - \frac{e^2 n}{T_i} \left(\alpha |\delta \phi|^2 - \frac{\Delta \tau}{2} \delta \phi^* \int_{1/B_{\max}}^{1/B(l)} \frac{B \, \mathrm{d}\lambda}{\sqrt{1 - \lambda B}} \overline{\delta \phi} \right) \right\rangle,
\tag{A1}
$$

where we have defined $\alpha = 1 + \tau + \Delta(1 + \tau - \Gamma_{0i})$. Written in this form, all that remains is to insert $\delta \phi$ from quasineutrality,

$$
\delta \phi = \frac{T_i}{en(1 + \tau)} \left(\int g_i \mathrm{J}_{0i} \, \mathrm{d}^3 v - \int g_e \, \mathrm{d}^3 v \right),
\tag{A2}
$$

and perform the variation over g_i and g_e, writing the result in terms of the inner product defined for each species given by (5.3) and (5.4) yielding

$$
\frac{\delta \tilde{H}}{\delta g_i} = \left\langle \left\langle \int \mathrm{d}^3 v \, \frac{T_i}{F_{i0}} g_i^* \left\{ \sum_b \tilde{\mathcal{H}}_{\mathrm{ib}} g_b \right\} \right\rangle \right\rangle + \mathrm{c.c.},
\tag{A3}
$$

and

$$
\frac{\delta \tilde{H}}{\delta g_e} = \frac{2\pi}{V} \sum_j \int_{1/B_{\max}}^{1/B_{\min}} \mathrm{d}\lambda \int_0^\infty \mathrm{d}v \, v^2 \tau_{B,j} \frac{T_e}{F_{e0}} g_e^* \left\{ \sum_b \tilde{\mathcal{H}}_{\mathrm{eb}} g_b \right\} + \mathrm{c.c.},
\tag{A4}
$$

from which the operators can be identified. The construction of the operators associated with D proceeds similarly. However, due to the derivatives with respect to l, care must be taken when finding the operators associated with K. This involves integration by parts,

and because the derivatives with l are taken at constant E_a and μ_a, we require the identity given in an appendix of Plunk & Helander (2023),

$$\int v_\parallel \frac{\partial g_i}{\partial l} J_{0i} \, d^3v = B \frac{\partial}{\partial l}\left(\frac{1}{B}\int v_\parallel g_i \, d^3v\right) - \int v_\parallel g_i \frac{\partial J_{0i}}{\partial l} \, d^3v. \quad (A5)$$

After some manipulation, the Hermitian linear operators can be found to be

$$\sum_b \tilde{\mathcal{H}}_{ib} g_b = g_i - \frac{F_{i0} J_{0i}}{(1+\tau)^2}\left(\alpha(\kappa_{1i} - \kappa_{1e}) - \frac{\Delta\tau}{2}\int_{1/B_{\max}}^{1/B(l)} \frac{B \, d\lambda}{\sqrt{1-\lambda B}}(\bar{\kappa}_{1i} - \bar{\kappa}_{1e})\right), \quad (A6)$$

$$\sum_b \tilde{\mathcal{H}}_{eb} g_b = g_e + \frac{\tau F_{e0}}{(1+\tau)^2}\overline{\left(\alpha(\kappa_{1i} - \kappa_{1e}) - \frac{\Delta\tau}{2}\int_{1/B_{\max}}^{1/B(l)} \frac{B \, d\lambda}{\sqrt{1-\lambda B}}(\bar{\kappa}_{1i} - \bar{\kappa}_{1e})\right)}, \quad (A7)$$

$$\sum_b \mathcal{D}_{ib} g_b = \frac{i F_{i0} J_{0i}}{2(1+\tau)}\left(\omega_{*i}\left(1 + \eta_i\left(\frac{v^2}{v_{Ti}^2} - \frac{3}{2}\right)\right)(\kappa_{1i} - \kappa_{1e})\right.$$
$$\left. -\omega_{*i}(1 - 3\eta_i/2)\kappa_{1i} - \omega_{*i}\eta_i\kappa_{2i} + \omega_{*e}(1 - 3\eta_e/2)\kappa_{1e} + \omega_{*e}\eta_e\kappa_{2e}\right), \quad (A8)$$

$$\sum_b \mathcal{D}_{eb} g_b = -\frac{i\tau F_{e0}}{2(1+\tau)}\overline{\left(\omega_{*e}\left(1 + \eta_e\left(\frac{v^2}{v_{Te}^2} - \frac{3}{2}\right)\right)(\bar{\kappa}_{1i} - \bar{\kappa}_{1e})\right.}$$
$$\left.\overline{ +\omega_{*e}(1 - 3\eta_e/2)\bar{\kappa}_{1e} + \omega_{*e}\eta_e\bar{\kappa}_{2e} - \omega_{*i}(1 - 3\eta_i/2)\bar{\kappa}_{1i} - \omega_{*i}\eta_i\bar{\kappa}_{2i}}\right), \quad (A9)$$

$$\sum_b \mathcal{K}_{ib} g_b = \frac{F_{i0}}{2(1+\tau)}\left(-J_{0i}B\frac{\partial}{\partial l}\left(\frac{v_{Ti}}{B}\kappa_{4i}\right) + v_{Ti}\kappa_{5i} + v_\parallel \frac{\partial}{\partial l}(J_{0i}(\kappa_{1i} - \kappa_{1e}))\right.$$
$$\left. -iJ_{0i}\left[\hat{\omega}_{di}(l)\kappa_{3i} - \tilde{\omega}_{de}\kappa_{3e} - \hat{\omega}_{di}(l)\left(\frac{v_\perp^2}{2v_{Ti}^2} + \frac{v_\parallel^2}{v_{Ti}^2}\right)(\kappa_{1i} - \kappa_{1e})\right]\right), \quad (A10)$$

$$\sum_b \mathcal{K}_{eb} g_b = \frac{\tau F_{e0}}{2(1+\tau)}\overline{\left(B\frac{\partial}{\partial l}\left(\frac{v_{Ti}}{B}\kappa_{4i}\right) - v_{Ti}\overline{\kappa_{5i}} + i\left[\hat{\omega}_{di}(l)\kappa_{3i}\right.\right.}$$
$$\left.\left.\overline{ -\tilde{\omega}_{de}\bar{\kappa}_{3e} - \hat{\omega}_{de}(l)\left(\frac{v_\perp^2}{2v_{Te}^2} + \frac{v_\parallel^2}{v_{Te}^2}\right)(\bar{\kappa}_{1i} - \bar{\kappa}_{1e})\right]}\right), \quad (A11)$$

where we have used the moment representation given by (5.6)–(5.11). Inserting these operators into (5.5), for $a = i$ and $a = e$, gives the equation for the optimal distribution function for ions and electrons, respectively.

Appendix B. Moment form of eigenvalue problem

Here, we give the (quite lengthy) closed set of equations which arise upon taking moments of (5.5). The moment equations which come from the optimal ion distribution

function equation are

$$
2\Lambda \left((1 + \tau)\kappa_{1i} - \frac{G_0}{(1 + \tau)} \left\{ \alpha(\kappa_{1i} - \kappa_{1e}) - \frac{\Delta\tau}{2} \int_{1/B_{\max}}^{1/B(l)} \frac{B(l)\,\mathrm{d}\lambda}{\sqrt{1 - \lambda B}} (\bar{\kappa}_{1i} - \bar{\kappa}_{1e}) \right\} \right)
$$

$$
= \mathrm{i} \left(\omega_{*i}\eta_i G_1(\kappa_{1i} - \kappa_{1e}) - \omega_{*i}\eta_i G_0 \kappa_{2i} - \omega_{*i}(1 - 3\eta_i/2)G_0 \kappa_{1e} + \omega_{*e}\eta_e G_0 \kappa_{2e} \right.
$$

$$
\left. + \omega_{*e}(1 - 3\eta_e/2)G_0 \kappa_{1e} - \Delta \left\{ \hat{\omega}_{\mathrm{di}}(l)G_3(\kappa_{1i} - \kappa_{1e}) + \tilde{\omega}_{\mathrm{de}} G_0 \kappa_{3e} - \hat{\omega}_{\mathrm{di}}(l)G_0 \kappa_{3i} \right\} \right),
$$

$$\text{(B1)}$$

$$
2\Lambda \left((1 + \tau)\kappa_{2i} - \frac{G_1}{(1 + \tau)} \left\{ \alpha(\kappa_{1i} - \kappa_{1e}) - \frac{\Delta\tau}{2} \int_{1/B_{\max}}^{1/B(l)} \frac{B(l)\,\mathrm{d}\lambda}{\sqrt{1 - \lambda B}} (\bar{\kappa}_{1i} - \bar{\kappa}_{1e}) \right\} \right)
$$

$$
= \mathrm{i} \left(\omega_{*i}\eta_i G_2(\kappa_{1i} - \kappa_{1e}) - \omega_{*i}\eta_i G_1 \kappa_{2i} - \omega_{*i}(1 - 3\eta_i/2)G_1 \kappa_{1e} + \omega_{*e}\eta_e G_1 \kappa_{2e} \right.
$$

$$
\left. + \omega_{*e}(1 - 3\eta_e/2)G_1 \kappa_{1e} - \Delta \left\{ \hat{\omega}_{\mathrm{di}}(l)G_4(\kappa_{1i} - \kappa_{1e}) + \tilde{\omega}_{\mathrm{de}} G_1 \kappa_{3e} - \hat{\omega}_{\mathrm{di}}(l)G_1 \kappa_{3i} \right\} \right),
$$

$$\text{(B2)}$$

$$
2\Lambda \left((1 + \tau)\kappa_{3i} - \frac{G_3}{(1 + \tau)} \left\{ \alpha(\kappa_{1i} - \kappa_{1e}) - \frac{\Delta\tau}{2} \int_{1/B_{\max}}^{1/B(l)} \frac{B(l)\,\mathrm{d}\lambda}{\sqrt{1 - \lambda B}} (\bar{\kappa}_{1i} - \bar{\kappa}_{1e}) \right\} \right)
$$

$$
= \mathrm{i} \left(\omega_{*i}\eta_i G_4(\kappa_{1i} - \kappa_{1e}) - \omega_{*i}\eta_i G_3 \kappa_{2i} - \omega_{*i}(1 - 3\eta_i/2)G_3 \kappa_{1e} + \omega_{*e}\eta_e G_3 \kappa_{2e} \right.
$$

$$
\left. + \omega_{*e}(1 - 3\eta_e/2)G_3 \kappa_{1e} - \Delta \left\{ \hat{\omega}_{\mathrm{di}}(l)G_5(\kappa_{1i} - \kappa_{1e}) + \tilde{\omega}_{\mathrm{de}} G_3 \kappa_{3e} - \hat{\omega}_{\mathrm{di}}(l)G_3 \kappa_{3i} \right\} \right). \text{ (B3)}
$$

Here, the functions $G_{ni} = G_{\mathrm{ni}}(b)$ come from evaluating the integrals over velocity space which contain J_{0i}^2 in the integrand. We use the same notation as was used in Part 3, where, in an appendix, these functions were computed and are given as

$$
G_0 = \Gamma_0, \tag{B4}
$$

$$
G_1 = \left(\tfrac{3}{2} - b\right)\Gamma_0 + b\Gamma_1, \tag{B5}
$$

$$
G_2 = \tfrac{1}{4}\left(\left(6b^2 - 20b + 15\right)\Gamma_0 + 2b\left((10 - 4b)\Gamma_1 + b\Gamma_2\right)\right), \tag{B6}
$$

$$
G_3 = \tfrac{1}{2}\left(b\Gamma_1 - (b - 2)\Gamma_0\right), \tag{B7}
$$

$$
G_4 = \tfrac{1}{4}\left(\left(3b^2 - 11b + 10\right)\Gamma_0 + b\left((11 - 4b)\Gamma_1 + b\Gamma_2\right)\right), \tag{B8}
$$

$$
G_5 = \tfrac{1}{8}\left(\left(3b^2 - 12b + 14\right)\Gamma_0 + b\left(b\Gamma_2 - 4(b - 3)\Gamma_1\right)\right), \tag{B9}
$$

where $\Gamma_n(b) = \mathrm{I}_n(b)\exp(-b)$ and I_n is the modified Bessel function of the first kind.

The equations which arise upon taking velocity space moments of the optimal electron distribution are

$$
2\Lambda\Bigg((1+\tau)\kappa_{1e} + \frac{\tau}{2(1+\tau)}\int_{1/B_{\max}}^{1/B(l)}\frac{B(l)\,\mathrm{d}\lambda}{\sqrt{1-\lambda B}}\Bigg\{\overline{\alpha(\kappa_{1i}-\kappa_{1e})}
$$
$$
-\frac{\Delta\tau}{2}\overline{\int_{1/B_{\max}}^{1/B(l)}\frac{B(l)\,\mathrm{d}\lambda}{\sqrt{1-\lambda B}}(\bar{\kappa}_{1i}-\bar{\kappa}_{1e})}\Bigg\}\Bigg)
$$
$$
=\frac{\tau i}{2}\int_{1/B_{\max}}^{1/B(l)}\frac{B(l)\,\mathrm{d}\lambda}{\sqrt{1-\lambda B}}\Bigg(\frac{3}{2}\omega_{*e}\eta_e(\bar{\kappa}_{1e}-\bar{\kappa}_{1i})
$$
$$
-\omega_{*e}(1-3\eta_e/2)\bar{\kappa}_{1i}-\omega_{*e}\eta_e\bar{\kappa}_{2e}+\omega_{*i}(1-3\eta_i/2)\bar{\kappa}_{1i}+\omega_{*i}\eta_i\bar{\kappa}_{2i}
$$
$$
-\Delta\Bigg\{\overline{\hat{\omega}_{\mathrm{di}}\kappa_{3i}}-\tilde{\omega}_{\mathrm{de}}\bar{\kappa}_{3e}-\frac{3}{2}\overline{\hat{\omega}_{\mathrm{de}}(1-\lambda B/2)}(\bar{\kappa}_{1i}-\bar{\kappa}_{1e})\Bigg\}\Bigg), \tag{B10}
$$

$$
2\Lambda\Bigg((1+\tau)\kappa_{2e} + \frac{3\tau}{4(1+\tau)}\int_{1/B_{\max}}^{1/B(l)}\frac{B(l)\,\mathrm{d}\lambda}{\sqrt{1-\lambda B}}\Bigg\{\overline{\alpha(\kappa_{1i}-\kappa_{1e})}
$$
$$
-\frac{\Delta\tau}{2}\overline{\int_{1/B_{\max}}^{1/B(l)}\frac{B(l)\,\mathrm{d}\lambda}{\sqrt{1-\lambda B}}(\bar{\kappa}_{1i}-\bar{\kappa}_{1e})}\Bigg\}\Bigg)
$$
$$
=\frac{3\tau i}{4}\int_{1/B_{\max}}^{1/B(l)}\frac{B(l)\,\mathrm{d}\lambda}{\sqrt{1-\lambda B}}\Bigg(\frac{5}{2}\omega_{*e}\eta_e(\bar{\kappa}_{1e}-\bar{\kappa}_{1i})
$$
$$
-\omega_{*e}(1-3\eta_e/2)\bar{\kappa}_{1i}-\omega_{*e}\eta_e\bar{\kappa}_{2e}+\omega_{*i}(1-3\eta_i/2)\bar{\kappa}_{1i}+\omega_{*i}\eta_i\bar{\kappa}_{2i}
$$
$$
-\Delta\Bigg\{\overline{\hat{\omega}_{\mathrm{di}}\kappa_{3i}}-\tilde{\omega}_{\mathrm{de}}\bar{\kappa}_{3e}-\frac{5}{2}\overline{\hat{\omega}_{\mathrm{de}}(1-\lambda B/2)}(\bar{\kappa}_{1i}-\bar{\kappa}_{1e})\Bigg\}\Bigg), \tag{B11}
$$

$$
2\Lambda\Bigg((1+\tau)\kappa_{3e} + \frac{3\tau}{4(1+\tau)}\int_{1/B_{\max}}^{1/B(l)}\frac{B(l)\,\mathrm{d}\lambda}{\sqrt{1-\lambda B}}\overline{f(l)(1-\lambda B/2)}\Bigg\{\overline{\alpha(\kappa_{1i}-\kappa_{1e})}
$$
$$
-\frac{\Delta\tau}{2}\overline{\int_{1/B_{\max}}^{1/B(l)}\frac{B(l)\,\mathrm{d}\lambda}{\sqrt{1-\lambda B}}(\bar{\kappa}_{1i}-\bar{\kappa}_{1e})}\Bigg\}\Bigg)
$$
$$
=\frac{3\tau i}{4}\int_{1/B_{\max}}^{1/B(l)}\frac{B(l)\,\mathrm{d}\lambda}{\sqrt{1-\lambda B}}\overline{f(l)(1-\lambda B/2)}
$$
$$
\times\Bigg(\frac{5}{2}\omega_{*e}\eta_e(\bar{\kappa}_{1e}-\bar{\kappa}_{1i})-\omega_{*e}(1-3\eta_e/2)\bar{\kappa}_{1i}-\omega_{*e}\eta_e\bar{\kappa}_{2e}+\omega_{*i}(1-3\eta_i/2)\bar{\kappa}_{1i}
$$
$$
+\omega_{*i}\eta_i\bar{\kappa}_{2i}-\Delta\Bigg\{\overline{\hat{\omega}_{\mathrm{di}}\kappa_{3i}}-\tilde{\omega}_{\mathrm{de}}\bar{\kappa}_{3e}-\frac{5}{2}\overline{\hat{\omega}_{\mathrm{de}}(1-\lambda B/2)}(\bar{\kappa}_{1i}-\bar{\kappa}_{1e})\Bigg\}\Bigg). \tag{B12}
$$

Appendix C. Eigenvalue problem in the square magnetic well

In the slow-ion-transit limit with a square magnetic trapping well, the *l*-dependence of the eigenvalue problem (5.5) is trivial. This makes the system of moment equations purely algebraic, allowing us to adopt a 'supermoment' representation akin to that of Part 2. We

define

$$\sigma_a = e_a n \left(\sum_a \frac{n e_a^2}{T_a} \right)^{-1/2}, \tag{C1}$$

$$\tilde{\kappa}_1 = \sum_a \sigma_a \kappa_{1a}, \tag{C2}$$

$$\tilde{\kappa}_2 = \sum_a \sigma_a \omega'_{*a} \left((1 - 3\eta_a/2) \right) \kappa_{1a} + \eta_a \kappa_{2a}), \tag{C3}$$

$$\tilde{\kappa}_3 = \sum_a \sigma_a \omega'_{da} \kappa_{3a}, \tag{C4}$$

where we have introduced the normalisation $\omega'_{*a} = \omega_{*a}/\omega_{*i}$ and $\omega'_{da} = \hat{\omega}_{da}/\omega_{*i}$. We may also define the following velocity-space-dependent factors:

$$\psi_{1a} = \mathrm{J}_{0a} \quad \psi_{2a} = \frac{v^2}{v_{\mathrm{Ta}}^2} \mathrm{J}_{0a} \tag{C5a,b}$$

$$\psi_{3a} = \left(\frac{v_\perp^2}{2 v_{Ta}^2} + \frac{v_\parallel^2}{v_{Ta}^2} \right) \mathrm{J}_{0a}, \tag{C6}$$

where we once again take $\mathrm{J}_{0e} \approx 1$. If we adopt the compact notation

$$\tilde{\kappa}_m = \sum_{n,b} c_{mn}^{(b)} \kappa_{nb}, \quad \mathcal{I}_{mn}^{(a)} = \frac{c_{mn}^{(a)} \sigma_a}{n T_a}, \tag{C7a,b}$$

then (5.5) for the species 'a' can be written as

$$\frac{\Lambda}{\omega_{*i}} \left(g_a + \frac{\tilde{\alpha} F_{a0}}{n T_a} \left(-\sigma_a \psi_{1a} \tilde{\kappa}_1 \right) \right) = \frac{\mathrm{i}}{2} \frac{F_{a0}}{n T_a} \left(\omega'_{*a} (1 - 3\eta_a/2) \sigma_a \psi_{1a} \tilde{\kappa}_1 + \omega'_{*a} \eta_a \sigma_a \psi_{2a} \tilde{\kappa}_1 \right.$$
$$\left. - \sigma_a \psi_{1a} \tilde{\kappa}_2 - \Delta \left[\sigma_a \omega'_{da} \psi_{3a} \tilde{\kappa}_1 - \sigma_a \psi_{1a} \tilde{\kappa}_3 \right] \right). \tag{C8}$$

Here, we have evaluated the integral,

$$\int_{1/B_{\mathrm{max}}}^{1/B(l)} \frac{B(l) \, \mathrm{d}\lambda}{\sqrt{1 - \lambda B}} = 2 \sqrt{1 - \frac{B(l)}{B_{\mathrm{max}}}} = 2\varepsilon(l) \tag{C9}$$

and defined $\tilde{\alpha} = (\alpha - \Delta \tau \varepsilon(l))/(1 + \tau)$. We can take moments of (C8) by multiplying by the constant $c_{mn}^{(a)}$ and the function ψ_{ma}, summing over the index n and the species label, and integrating over velocity space to arrive at

$$\frac{\Lambda}{\omega_{*i}} \left(\tilde{\kappa}_m + \tilde{\alpha} \sum_{a,n} \left\{ \mathcal{I}_{mn}^{(a)} X_{1n}^{(a)} \tilde{\kappa}_1 \right\} \right)$$
$$= \sum_{a,n} \frac{\mathrm{i}}{2} \left(\omega'_{*a} (1 - 3\eta_a/2) \mathcal{I}_{mn}^{(a)} X_{1n}^{(a)} \tilde{\kappa}_1 + \omega'_{*a} \eta_a \mathcal{I}_{mn}^{(a)} X_{2n}^{(a)} \tilde{\kappa}_1 - \mathcal{I}_{mn}^{(a)} X_{1n}^{(a)} \tilde{\kappa}_2 \right.$$
$$\left. - \Delta \left[\omega'_{da} \mathcal{I}_{mn}^{(a)} X_{3n}^{(a)} \tilde{\kappa}_1 - \mathcal{I}_{mn}^{(a)} X_{1n}^{(a)} \tilde{\kappa}_3 \right] \right), \tag{C10}$$

where the factors $X_{\mathrm{mn}}^{(a)}$ are integrals over velocity space defined by

$$X_{\mathrm{mn}}^{(a)} = \frac{1}{n} \int F_{0a} \psi_{\mathrm{ma}} \psi_{\mathrm{na}} J_{0a} \, \mathrm{d}^3 v, \tag{C11}$$

where, for the electron species, the velocity space integral is carried out in the trapped region of velocity space, defined by $1/B_{\max} \leqslant \lambda \leqslant 1/B_{\min}$.

Written in this form, the system reduces to a simple 3×3 generalised eigenvalue problem which may be solved for the eigenvalue Λ. The $X_{nm}^{(a)}$s are given by

$$X_{11}^{(e)} = \varepsilon, \quad X_{11}^{(i)} = G_0(b), \tag{C12a,b}$$

$$X_{12}^{(e)} = \tfrac{3}{2}\varepsilon, \quad X_{12}^{(i)} = G_1(b), \tag{C13a,b}$$

$$X_{13}^{(e)} = \tfrac{3}{4}\left(\varepsilon + \tfrac{1}{3}\varepsilon^3\right), \quad X_{13}^{(i)} = G_3(b), \tag{C14a,b}$$

$$X_{22}^{(e)} = \tfrac{15}{4}\varepsilon, \quad X_{22}^{(i)} = G_2(b), \tag{C15a,b}$$

$$X_{32}^{(e)} = \tfrac{15}{8}\left(\varepsilon + \tfrac{1}{3}\varepsilon^3\right), \quad X_{32}^{(i)} = G_4(b), \tag{C16a,b}$$

$$X_{33}^{(e)} = \frac{15}{8}\left(\frac{\varepsilon}{2} + \frac{1}{3}\varepsilon^3 + \frac{1}{10}\varepsilon^5\right), \quad X_{33}^{(i)} = G_5(b), \tag{C17a,b}$$

where the functions $G_n(b)$ are given in appendix B. In this simple limit, the eigenvalue problem can be solved analytically to yield

$$\begin{aligned}
\Lambda_{\mathrm{SW}}^2 = (&C_{\mathrm{ee}}^{**}\omega_{*e}^2 + C_{\mathrm{ie}}^{**}\omega_{*e}\omega_{*i} + C_{\mathrm{ii}}^{**}\omega_{*i}^2 + C_{\mathrm{ii}}^{*d}\omega_{*i}\hat{\omega}_{\mathrm{di}} + C_{\mathrm{ii}}^{dd}\hat{\omega}_{\mathrm{di}}^2 + C_{\mathrm{ee}}^{*d}\omega_{*e}\hat{\omega}_{\mathrm{de}} + C_{\mathrm{ee}}^{dd}\hat{\omega}_{\mathrm{de}}^2 \\
&+ C_{\mathrm{ie}}^{*d}\omega_{*i}\hat{\omega}_{\mathrm{de}} + C_{\mathrm{ie}}^{d*}\omega_{*e}\hat{\omega}_{\mathrm{di}} + C_{\mathrm{ie}}^{dd}\hat{\omega}_{\mathrm{de}}\hat{\omega}_{\mathrm{di}})/(16(1+\tau)(1+\tau-\tilde{\alpha}(X_{11}^{(i)} + \tau X_{11}^{(e)}))),
\end{aligned} \tag{C18}$$

where we define the following factors:

$$C_{\mathrm{ee}}^{**} = \tau X_{11}^{(e)}((2-3\eta_e)^2)X_{11}^{(i)} + 4\tau\eta_e^2 X_{22}^{(e)}) + 4\tau\eta_e(X_{11}^{(i)}((2-3\eta_e)X_{12}^{(e)} + \eta_e X_{22}^{(e)}) - \tau\eta_e X_{12}^{(e)^2}), \tag{C19}$$

$$C_{\mathrm{ie}}^{**} = -2\tau((3\eta_e-2)X_{11}^{(e)} - 2\eta_e X_{12}^{(e)})((3\eta_i-2)X_{11}^{(i)} - 2\eta_i X_{12}^{(i)}), \tag{C20}$$

$$C_{\mathrm{ii}}^{**} = \tau X_{11}^{(e)}((2-3\eta_i)^2 X_{11}^{(i)} + 4\eta_i((2-3\eta_i)X_{12}^{(i)} + \eta_i X_{22}^{(i)})) - 4\eta_i^2(X_{12}^{(i)^2} - X_{11}^{(i)}X_{22}^{(i)}), \tag{C21}$$

$$C_{\mathrm{ii}}^{*d} = 4\Delta(2\eta_i(X_{12}^{(i)}X_{13}^{(i)} - X_{11}^{(i)}X_{23}^{(i)}) + \tau X_{11}^{(e)}((3\eta_i-2)X_{13}^{(i)} - 2X_{23}^{(i)}\eta_i)), \tag{C22}$$

$$C_{\mathrm{ii}}^{dd} = 4\Delta^2(X_{33}^{(i)}(X_{11}^{(i)} + \tau X_{11}^{(e)}) - X_{13}^{(i)^2}), \tag{C23}$$

$$C_{\mathrm{ee}}^{*d} = 4\Delta\tau(X_{11}^{(i)}((3\eta_e-2)X_{13}^{(e)} - 2\eta_e X_{23}^{(e)}) + 2\tau\eta_e(X_{12}^{(e)}X_{13}^{(e)} - X_{11}^{(e)}X_{23}^{(e)})), \tag{C24}$$

$$C_{\mathrm{ee}}^{dd} = 4\Delta^2\tau(X_{33}^{(e)}(X_{11}^{(i)} + \tau X_{11}^{(e)}) - \tau X_{13}^{(e)^2}), \tag{C25}$$

$$C_{\mathrm{ie}}^{d*} = 4\Delta\tau(X_{13}^{(i)}(X_{11}^{(e)}(2-3\eta_e) + 2X_{12}^{(e)}\eta_e)), \tag{C26}$$

$$C_{\mathrm{ie}}^{*d} = 4\Delta\tau((X_{13}^{(e)}((X_{11}^{(i)}(2-3\eta_i) + 2(X_{12}^{(i)}\eta_i)), \tag{C27}$$

$$C_{\mathrm{ie}}^{dd} = -8\tau\Delta^2 X_{13}^{(i)}X_{13}^{(e)}. \tag{C28}$$

Appendix D. Linear theory

To make a comparison between the upper bounds derived here in the bounce-averaged electron response limit, we must solve the integral equation

$$(1 + \tau - R_i(\xi_i, l))\phi = \tau \int_{1/B_{\max}}^{1/B(l)} \frac{B(l)\,\mathrm{d}\lambda}{\sqrt{1 - \lambda B}} R_e(\lambda, \xi_e)\bar{\phi}, \tag{D1}$$

where $\xi_i = \omega/\hat{\omega}_{\mathrm{di}}(l)$, $\xi_e = \omega/(\overline{\hat{\omega}_{\mathrm{de}}(1 - \lambda B/2)})$ and the ion response R_i is given by the standard expression of Biglari *et al.* (1989),

$$R_i(\xi_i, l) = Y(\xi_i)^2 + \kappa_{\mathrm{di}}\left\{\left[\frac{\eta_i - 1}{\xi_i} - 2\eta_i\right]Y(\xi_i)^2 + 2\eta_i Y(\xi_i)\right\}, \tag{D2}$$

where $\kappa_{\mathrm{di}} = \omega_{*i}/\hat{\omega}_{\mathrm{di}}(l)$ and $Y(\xi_i) = -\sqrt{\xi_i}Z(\sqrt{\xi_i})$ with Z being the plasma dispersion function and where the principal branch of $\sqrt{\xi_i}$ has been selected. The electron response function R_e is

$$R_e(\lambda, \xi_e) = \frac{2}{\sqrt{\pi}} \int_0^\infty x^2 \mathrm{e}^{-x^2}\left(\frac{\xi_e - \kappa_{\mathrm{de}}}{\xi_e - x^2}\right)\mathrm{d}x, \tag{D3}$$

where $x = v/v_{\mathrm{Te}}$, $\kappa_{\mathrm{de}} = \omega_{*e}/(\overline{\hat{\omega}_{\mathrm{de}}(1 - \lambda B/2)})$ and we have taken $\eta_e = 0$ for simplicity. Here, because the integrand is even in x, the integration domain can be extended to $x \in [-\infty, \infty]$. Additionally, a partial fraction expansion can be employed to yield

$$R_e(\lambda, \xi_e) = \frac{(\kappa_{\mathrm{de}} - \xi_e)}{\sqrt{\pi}} \frac{1}{2\sqrt{\xi_e}} \int_{-\infty}^\infty \mathrm{e}^{-x^2}\left(\frac{x^2}{x - \sqrt{\xi_e}} - \frac{x^2}{x + \sqrt{\xi_e}}\right)\mathrm{d}x,$$

where we have selected the principal branch of $\sqrt{\xi_e}$. The above integrals can be written in terms of the standard definition of the plasma dispersion function, but care must be taken. Because we are interested in unstable eigenmodes, defined as $\mathrm{Im}\,\xi_i > 0$ (which corresponds to $\mathrm{Im}\,\xi_e < 0$), we can express the integral in terms of the plasma dispersion function by evaluating Z in the complex-conjugate plane when the imaginary component of its argument is negative and then taking the complex conjugate of the output. This avoids the contribution from analytic continuation into the lower-half of the complex plane which is included in the definition of Z but is not relevant here;

$$R_e(\xi_e, \lambda) = (\kappa_{\mathrm{de}} - \xi_e)\left\{1 + \frac{1}{2}\sqrt{\xi_e}\left[Z\left(-\sqrt{\xi_e}\right)\right]\right\}. \tag{D4}$$

Which is equivalent to previous derivations by Connor *et al.* (1980). For this work, we only consider the solution to this equation in a square magnetic trapping well with constant curvature. In this case, $\phi = \bar{\phi}$ and $\hat{\omega}_{da}(l) = \mathrm{const}$. The integral over λ and the roots of the dispersion relation can both be computed numerically. The solution is shown in figure 5.

REFERENCES

ALCUSÓN, J.A., XANTHOPOULOS, P., PLUNK, G.G., HELANDER, P., WILMS, F., TURKIN, Y., VON STECHOW, A. & GRULKE, O. 2020 Suppression of electrostatic micro-instabilities in maximum-J stellarators. *Plasma Phys. Control. Fusion* **62** (3), 035005.

BIGLARI, H., DIAMOND, P.H. & ROSENBLUTH, M.N. 1989 Toroidal ion-pressure-gradient-driven drift instabilities and transport revisited. *Phys. Fluids* B **1** (1), 109–118.

CONNOR, J.W., HASTIE, R.J. & TAYLOR, J.B. 1980 Stability of general plasma equilibria. III. *Plasma Phys.* **22** (7), 757.

COPPI, B. & PEGORARO, F. 1977 Theory of the ubiquitous mode. *Nucl. Fusion* **17** (5), 969.

DELSOLE, T. 2004 The necessity of instantaneous optimals in stationary turbulence. *J. Atmos. Sci.* **61** (9), 1086–1091.

DIAMOND, P.H., ITOH, S.-I., ITOH, K. & HAHM, T.S. 2005 Zonal flows in plasma—a review. *Plasma Phys. Control. Fusion* **47** (5), R35.

DORLAND, W., JENKO, F., KOTSCHENREUTHER, M. & ROGERS, B.N. 2000 Electron temperature gradient turbulence. *Phys. Rev. Lett.* **85** (26), 5579–5582.

GOODMAN, A.G., XANTHOPOULOS, P., PLUNK, G.G., SMITH, H., NÜHRENBERG, C., BEIDLER, C.D., HENNEBERG, S.A., ROBERG-CLARK, G., DREVLAK, M. & HELANDER, P. 2024 Quasi-isodynamic stellarators with low turbulence as fusion reactor candidates. *PRX Energy* **3** (2), 023010.

HELANDER, P. 2017 Available energy and ground states of collisionless plasmas. *J. Plasma Phys.* **83** (4), 715830401.

HELANDER, P. & NÜHRENBERG, J. 2009 Bootstrap current and neoclassical transport in quasi-isodynamic stellarators. *Plasma Phys. Control. Fusion* **51** (5), 055004.

HELANDER, P. & PLUNK, G.G. 2015 The universal instability in general geometry. *Phys. Plasmas* **22** (9), 090706.

HELANDER, P. & PLUNK, G.G. 2021 Upper bounds on gyrokinetic instabilities in magnetized plasmas. *Phys. Rev. Lett.* **127**, 155001.

HELANDER, P. & PLUNK, G.G. 2022 Energetic bounds on gyrokinetic instabilities. Part 1. Fundamentals. *J. Plasma Phys.* **88** (2), 905880207.

HELANDER, P., PROLL, J.H.E. & PLUNK, G.G. 2013 Collisionless microinstabilities in stellarators. I. Analytical theory of trapped-particle modes. *Phys. Plasmas* **20** (12), 122505.

LANDREMAN, M., PLUNK, G.G. & DORLAND, W. 2015 Generalized universal instability: transient linear amplification and subcritical turbulence. *J. Plasma Phys.* **81** (5), 905810501.

MACKENBACH, R.J.J., DUFF, J.M., GERARD, M.J., PROLL, J.H.E., HELANDER, P. & HEGNA, C.C. 2023*a* Bounce-averaged drifts: equivalent definitions, numerical implementations, and example cases. *Phys. Plasmas* **30** (9), 093901.

MACKENBACH, R.J.J., PROLL, J.H.E., WAKELKAMP, R. & HELANDER, P. 2023*b* The available energy of trapped electrons: a nonlinear measure for turbulent transport. *J. Plasma Phys.* **89** (5), 905890513.

NÜHRENBERG, J. 2010 Development of quasi-isodynamic stellarators. *Plasma Phys. Control. Fusion* **52** (12), 124003.

PLUNK, G.G., CONNOR, J.W. & HELANDER, P. 2017 Collisionless microinstabilities in stellarators. Part 4. The ion-driven trapped-electron mode. *J. Plasma Phys.* **83** (4), 715830404.

PLUNK, G.G. & HELANDER, P. 2022 Energetic bounds on gyrokinetic instabilities. Part 2. Modes of optimal growth. *J. Plasma Phys.* **88** (3), 905880313.

PLUNK, G.G. & HELANDER, P. 2023 Energetic bounds on gyrokinetic instabilities. Part 3. Generalized free energy. *J. Plasma Phys.* **89** (4), 905890419.

PLUNK, G.G., HELANDER, P., XANTHOPOULOS, P. & CONNOR, J.W. 2014 Collisionless microinstabilities in stellarators. III. The ion-temperature-gradient mode. *Phys. Plasmas* **21** (3), 032112.

PLUNK, G.G., *et al.* 2019 Stellarators resist turbulent transport on the electron larmor scale. *Phys. Rev. Lett.* **122** (3), 035002.

PODAVINI, L., PLUNK, G.G., HELANDER, P. & ZOCCO, A. 2025 Energetic bounds on gyrokinetic instabilities. Part 5. Contrasting optimal and normal modes over the geometric landscape. *J. Plasma Phys.* (In preparation).

PROLL, J.H.E., HELANDER, P., CONNOR, J.W. & PLUNK, G.G. 2012 Resilience of quasi-isodynamic stellarators against trapped-particle instabilities. *Phys. Rev. Lett.* **108** (24), 245002.

PROLL, J.H.E., PLUNK, G.G., FABER, B.J., GÖRLER, T., HELANDER, P., MCKINNEY, I.J., PUESCHEL, M.J., SMITH, H.M. & XANTHOPOULOS, P. 2022 Turbulence mitigation in maximum-J stellarators with electron-density gradient. *J. Plasma Phys.* **88** (1), 905880112.

RICCI, P., ROGERS, B.N., DORLAND, W. & BARNES, M. 2006 Gyrokinetic linear theory of the entropy mode in a *Z* pinch. *Phys. Plasmas* **13** (6), 062102.

ROBERG-CLARK, G.T., PLUNK, G.G., XANTHOPOULOS, P., NÜHRENBERG, C., HENNEBERG, S.A. & SMITH, H.M. 2023 Critical gradient turbulence optimization toward a compact stellarator reactor concept. *Phys. Rev. Res.* **5** (3), L032030.

RODRÍGUEZ, E., HELANDER, P. & GOODMAN, A.G. 2024 The maximum-J property in quasi-isodynamic stellarators. *J. Plasma Phys.* **90** (2), 905900212.

ROSENBLUTH, M.N. 1968 Low-frequency limit of interchange instability. *Phys. Fluids* **11** (4), 869–872.

SÁNCHEZ, E., VELASCO, J.L., CALVO, I. & MULAS, S. 2023 A quasi-isodynamic configuration with good confinement of fast ions at low plasma β. *Nucl. Fusion* **63** (6), 066037.